Remotely estimating total suspended solids concentration in clear to extremely turbid waters using a novel semi-analytical method

Dalin Jiang [a], Bunkei Matsushita [a,*], Nima Pahlevan [b,c], Daniela Gurlin [d], Moritz K. Lehmann [e], Cédric G. Fichot [f], John Schalles [g], Hubert Loisel [h], Caren Binding [i], Yunlin Zhang [j], Krista Alikas [k], Kersti Kangro [k], Mirjam Uusõue [k], Michael Ondrusek [l], Steven Greb [m], Wesley J. Moses [n], Steven Lohrenz [o], David O'Donnell [p]

[a] Faculty of Life and Environmental Sciences, University of Tsukuba, Ibaraki, Japan
[b] NASA Goddard Space Flight Center, Greenbelt, MD, USA
[c] Science Systems and Applications Inc., Lanham, MD, USA
[d] Wisconsin Department of Natural Resources, Madison, WI, USA
[e] Xerra Earth Observation Institute and the University of Waikato, Hamilton, New Zealand
[f] Department of Earth and Environment, Boston University, Boston, MA, USA
[g] Creighton University, Department of Biology, Omaha, NE, USA
[h] Univ. Littoral Côte d'Opale, Univ. Lille, CNRS, UMR 8187, LOG, Laboratoire d'Océanologie et de Géosciences, Lille, France
[i] Water Science and Technology Directorate, Environment and Climate Change Canada, Burlington, ON, Canada
[j] Taihu Lake Laboratory Ecosystem Research Station, State Key Laboratory of Lake Science and Environment, Nanjing Institute of Geography and Limnology, Chinese Academy of Sciences, Nanjing, China
[k] Tartu Observatory of the University of Tartu, Tartu, Estonia
[l] NOAA Center for Satellite Applications and Research, College Park, MD, USA
[m] University of Wisconsin-Madison, Space Science and Engineering, Madison, WI, USA
[n] Naval Research Laboratory, Washington, DC, USA
[o] School for Marine Science and Technology, University of Massachusetts Dartmouth, New Bedford, MA, USA
[p] Upstate Freshwater Institute, Syracuse, NY, USA

ARTICLE INFO

ABSTRACT

Total suspended solids (TSS) concentration is an important biogeochemical parameter for water quality management and sediment-transport studies. In this study, we propose a novel semi-analytical method for estimating TSS in clear to extremely turbid waters from remote-sensing reflectance (R_{rs}). The proposed method includes three sub-algorithms used sequentially. First, the remotely sensed waters are classified into clear (Type I), moderately turbid (Type II), highly turbid (Type III), and extremely turbid (Type IV) water types by comparing the values of R_{rs} at 490, 560, 620, and 754 nm. Second, semi-analytical models specific to each water type are used to determine the particulate backscattering coefficients (b_{bp}) at a corresponding single wavelength (*i.e.*, 560 nm for Type I, 665 nm for Type II, 754 nm for Type III, and 865 nm for Type IV). Third, a specific relationship between TSS and b_{bp} at the corresponding wavelength is used in each water type. Unlike other existing approaches, this method is strictly semi-analytical and its sub-algorithms were developed using synthetic datasets only. The performance of the proposed method was compared to that of three other state-of-the-art methods using simulated ($N = 1000$, TSS ranging from 0.01 to 1100 g/m^3) and *in situ* measured ($N = 3421$, TSS ranging from 0.09 to 2627 g/m^3) pairs of R_{rs} and TSS. Results showed a significant improvement with a Median Absolute Percentage Error (MAPE) of 16.0% *versus* 30.2–90.3% for simulated data and 39.7% *versus* 45.9–58.1% for *in situ* data, respectively. The new method was subsequently applied to 175 MEdium Resolution Imaging Spectrometer (MERIS) and 498 Ocean and Land Colour Instrument (OLCI) images acquired in the 2003–2020 timeframe to produce long-term TSS time-series for Lake Suwa and Lake Kasumigaura, Japan. Performance assessments using MERIS and OLCI matchups showed good agreements with *in situ* TSS measurements.

1. Introduction

The concentration of total suspended solids (TSS) influences water transparency, its aesthetic value, the transport and release of heavy metals and nutrients, light availability and its impact on the growth of aquatic organisms, aquatic ecosystem status, and fishery resources, and through increased absorption can affect water temperature. TSS is therefore an important biogeochemical parameter for water quality monitoring and water resource management (Bilotta and Brazier, 2008; Syvitski et al., 2005; Williamson and Crawford, 2011; Kroon et al., 2012). Since satellite remote sensing is a valuable and efficient tool for monitoring water quality at high temporal and spatial resolutions, many efforts have been made to accurately estimate TSS concentration from optical remote sensing data (e.g. Dekker et al., 2001; Miller and McKee, 2004; Kutser et al., 2007; Zhang et al., 2010; Mao et al., 2012; Ondrusek et al., 2012; Shi et al., 2015; Novoa et al., 2017; Yu et al., 2019; Balasubramanian et al., 2020).

Generally, there are two types of methods for estimating TSS from remote-sensing reflectance (R_{rs}) or water-leaving reflectance (ρ_w): (1) directly estimating TSS from one (or a combination of) R_{rs} or ρ_w band(s) (*e.g.*, Doxaran et al., 2002; Nechad et al., 2010; Chen et al., 2015; Knaeps et al., 2015; Han et al., 2016; Hou et al., 2017; Novoa et al., 2017; Yu et al., 2019); (2) estimating a proxy parameter, *e.g.* the particulate backscattering coefficients (b_{bp}) or water turbidity first and then the TSS concentration (*e.g.*, Binding et al., 2010; Neukermans et al., 2012; Alcântara et al., 2016; Balasubramanian et al., 2020; Xue et al., 2020; Dogliotti et al., 2015; Fichot et al., 2016). The use of b_{bp} as the proxy parameter for TSS has two advantages. First, b_{bp} is strongly correlated with TSS because interferences from colored dissolved organic matter (CDOM, a non-particulate optically-significant substance) and algal pigments on b_{bp} are limited (Schalles, 2006). Second, b_{bp} can be accurately estimated from R_{rs} using semi-analytical models for various waters (Lee et al., 2002; Yang et al., 2013; Jiang et al., 2019). Therefore, a b_{bp}-based TSS estimation method was promoted in a recent study (Balasubramanian et al., 2020). However, the empirical parameterizations of the algorithm for estimating b_{bp} in extremely turbid waters and relationship between b_{bp} and TSS will likely limit the applicability of this approach to a broad range of water types.

To develop a TSS estimation method applicable to a wide range of waters, previous studies suggested using R_{rs} at multiple wavelengths (bands). For example, Novoa et al. (2017) developed a three-band-switching method to estimate the TSS concentrations from ρ_w. To avoid ρ_w saturation effects in waters with high TSS concentration, they selected a TSS-sensitive band from those centered at 551, 671 and 862 nm according to threshold values of $\rho_w(671)$. Yu et al. (2019) proposed an empirical Globally Applicable Algorithm (GAA) for estimating TSS concentration from R_{rs} at four wavelengths (551, 671, 745, and 862 nm). The GAA method used the ratios [$R_{rs}(671)$, $R_{rs}(745)$, $R_{rs}(862)$]/$R_{rs}(551)$ with progressively adjusted weights to ensure a seamless retrieval of TSS. Moreover, Balasubramanian et al. (2020) suggested using b_{bp} at 665 and 740 nm to estimate TSS following a water type classification.

Most multi-wavelength methods require a water type classification algorithm to initially determine the most appropriate wavelength(s) and the corresponding algorithm for accurately estimating water quality parameters (Fichot et al., 2008; Vantrepotte et al., 2012; Moore et al., 2014; Matsushita et al., 2015; Novoa et al., 2017; Neil et al., 2019; Balasubramanian et al., 2020). However, these water type classification algorithms were developed using different *in situ*-measured datasets and with different research purposes, and thus their water type classification results may not be suitable for estimating TSS concentration in a broad range of water types.

Consequently, the objectives of the present study are to: (1) propose a widely applicable multi-wavelength-based semi-analytical method for estimating TSS concentrations in clear to extremely turbid waters by using two large synthetic datasets; (2) validate the proposed method using simulated ($N = 1000$), *in situ*-measured ($N = 3421$), and satellite-derived ($N = 170$) R_{rs} spectra and corresponding TSS data; (3) apply the proposed method to MEdium Resolution Imaging Spectrometer (MERIS, 2003–2012) and Ocean and Land Colour Instrument (OLCI, 2016–2020) satellite images to obtain long-term TSS time-series for Lake Suwa and Lake Kasumigaura, Japan; and (4) demonstrate the performance of the proposed method in three large river estuaries (Nile River, Amazon River, and Yangtze River) and four lakes (Lake Victoria, Lake Qinghai, Lake Turkana, and Lake Kasumigaura).
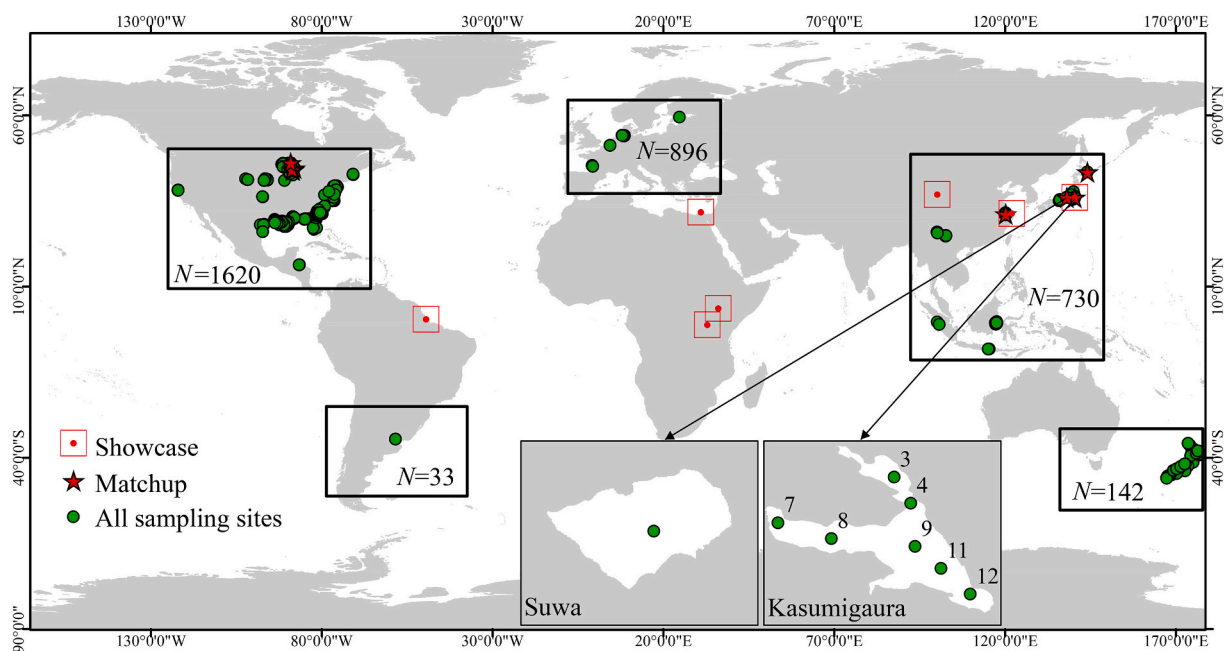

Fig. 1. Locations of water sampling. Green circles represent sampling points, red stars represent matchups with satellite images, red rectangles represent the water bodies for TSS estimation showcases. (For interpretation of the references to colour in this figure legend, the reader is referred to the web version of this article.)
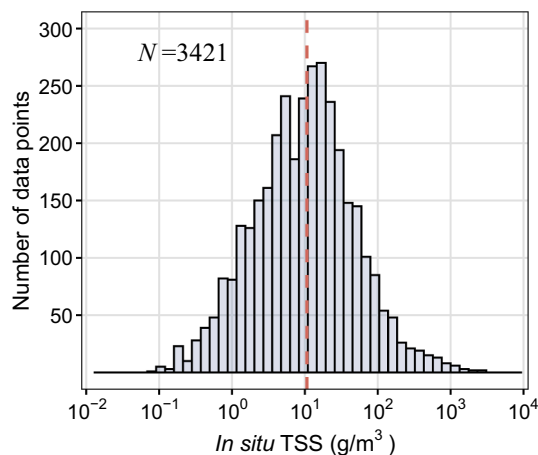
Fig. 2. Distribution of TSS concentrations in the *In Situ* Dataset used in this study. The red dashed line represents the median TSS concentration. (For interpretation of the references to colour in this figure legend, the reader is referred to the web version of this article.)

2. Data acquisition

2.1. In situ data collection and post-processing

In total, we compiled 3421 *in situ*-measured hyperspectral R_{rs} (wavelength dependence, λ, is omitted for brevity) and TSS data pairs from inland and coastal waters around the world (Fig. 1, hereafter as *In Situ* Dataset). The TSS concentrations were measured gravimetrically based on standard protocols (filtering of a water sample onto a pre-weighted glass-fiber filter, drying, and subsequent weighing; APHA 2540, 2005; Strickland and Parsons, 1972). The TSS data ranged from 0.09 g/m³ to 2627 g/m³ with a median value of ~10 g/m³, which covered clear to extremely turbid waters (Fig. 2). About 80% of the compiled data are the same as the validation data used in Balasubramanian et al. (2020) with chlorophyll-*a* concentrations ranging from 0.02 mg/m³ to 490 mg/m³ (mean and median values are 19.9 mg/m³ and 6.52 mg/m³, respectively). For the remaining data, chlorophyll-*a* concentrations ranged from 0.55 mg/m³ to 943 mg/m³ with a mean value of 41 mg/m³.

The *in situ*-measured R_{rs} were obtained through three approaches: (1) above-water approach ($N = 1110$, Mobley, 1999); (2) in-water approach ($N = 2212$, Gurlin et al., 2011; Fritz et al., 2017); and (3) skylight-blocked approach ($N = 99$, Lee et al., 2013) (Table 1). The first approach directly measures the total upwelling radiance (L_t), the downwelling irradiance (E_d^{0+}) and the radiance of skylight (L_{sky}) just above the water surface, with R_{rs} then calculated using the ratio ($L_t - \rho L_{sky}$)/ E_d^{0+}, (where ρ is the water surface reflectance factor). The second approach directly measures the upwelling radiance below the water surface (L_u^{0-}) and E_d^{0+}. The water leaving radiance (L_w) is obtained by correcting for the air-water interface effects (*i.e.*, $L_w = L_u^{0-} \times t/n^2$, where $t = 0.98$ is the water-to-air transmittance, and $n = 1.33$ is the refractive

index of water relative to air; Mobley, 1994; Gitelson et al., 2009). The R_{rs} is calculated as the ratio L_w/ E_d^{0+}. The third approach directly measures the L_w by using a tube in front of the radiance sensor to block the skylight and E_d^{0+}. The R_{rs} is then calculated as the ratio L_w/ E_d^{0+}, and corrected to remove the influence of instrument shadow using the method proposed by Shang et al. (2017). In addition, 20 R_{rs} spectra were obtained from airborne imagery with the Portable Remote Imaging SpectroMeter (PRISM), for which atmospheric correction was performed using a modified ATmosphere REMoval Program (ATREM, Thompson et al., 2015; Fichot et al., 2016). Although the imagery was acquired at low altitude (~6100 m) during very clear atmospheric conditions, these R_{rs} spectra contain some uncertainty resulting from atmospheric correction.

Previous studies have reported that R_{rs} observations collected using the above-water approach usually suffer from the effects of residual reflected skylight (Lee et al., 2010; Jiang et al., 2020). Therefore, R_{rs} spectra obtained with the above-water approach were further corrected using a method proposed by Jiang et al. (2020, N=943). Spectra acquired from the SeaSWIR database ($N = 137$) were already corrected by the data provider (Knaeps et al., 2018). A further 30 spectra (with TSS ranging from 1.8 g/m³ to 57.8 g/m³ with a mean value of 12.1 g/m³) were corrected following Ruddick et al. (2005), as these R_{rs} spectra don't have the 810 and 840 nm wavelengths which are required in the method of Jiang et al. (2020).

This large dataset was used to evaluate the performance of the proposed TSS estimation method.

We additionally acquired two long-term *in situ*-measured TSS datasets from Lake Kasumigaura and Lake Suwa in Japan to further evaluate the estimated TSS concentration from MERIS and OLCI images. For Lake Kasumigaura, monthly *in situ*-measured TSS data collected between January 2003 and March 2020 from seven sites (Fig. 1) were obtained from the National Institute for Environmental Studies, Japan database ($N = 1449$, NIES, 2020). For Lake Suwa, the almost weekly *in situ*-measured TSS data from April 2003 to July 2020 at the center of the lake were provided by Shinshu University, Japan ($N = 715$, Fig. 1).

2.2. Synthetic data generation

In this study, we generated three synthetic datasets: (1) Synthetic Dataset I was used to build relationships between TSS and b_{bp}, (2) Synthetic Dataset II was used to develop an algorithm for water type classification, and (3) Synthetic Dataset III was used to validate the new TSS estimation method.

Synthetic Dataset I contains pairs of TSS concentration and corresponding b_{bp} values. The b_{bp} can be expressed as (Kutser et al., 2001; Vahtmäe et al., 2006; Yang et al., 2011):

$$b_{bp}(\lambda) = C_{chl} \cdot b_{bph}^*(\lambda) + C_{tr} \cdot b_{btr}^*(\lambda), \tag{1}$$

where C_{chl} and C_{tr} are the concentrations of chlorophyll-*a* (Chl-*a*) and tripton (or non-algal particles, NAP), respectively. Here, b^*_{bph} and b^*_{btr} are the mass-specific backscattering coefficients of phytoplankton and tripton, respectively, and can be modeled using a power-law function (*e.*

Table 1
Summary of the spectral data collected in this study.

Approach	Number of data	Min. TSS (g/m³)	Mean TSS (g/m³)	Max. TSS (g/m³)	Equipment used	Residual reflected skylight correction	Reference
Above-water	1110	0.36	57.68	1400.54	ASD FieldSpec HandHeld, TriOS RAMSES, JPL/NASA PRISM	Yes	Matsushita et al., 2015; Shi et al., 2015; Fichot et al., 2016; Knaeps et al., 2018; Alikas et al., 2020; Jiang et al., 2020
In-water	2212	0.09	29.23	2626.82	TriOS RAMSES, Satlantic HyperPRO, Ocean Optics USB2000 and USB 2000+	No	Gurlin et al., 2011; Fritz et al., 2017; Binding et al., 2019
Skylight-blocked	99	0.10	4.20	83.20	Satlantic HyperOCR	No	Personal communication

Table 2
The ranges, intervals, numbers, and references for all input parameters used to generate Synthetic Dataset I.

Parameter	Range	Interval	Number	Reference
C_{chl}	0.02–0.1 mg/m³	0.02 mg/m³	25	
	0.2–1 mg/m³	0.2 mg/m³		
	2–10 mg/m³	2 mg/m³		
	20–100 mg/m³	20 mg/m³		
	200–1000 mg/m³	200 mg/m³		
C_{tr}	0.02–0.1 g/m³	0.02 g/m³	25	
	0.2–1 g/m³	0.2 g/m³		
	2–10 g/m³	2 g/m³		
	20–100 g/m³	20 g/m³		
	200–1000 g/m³:	200 g/m³		
$b^*_{bph}(550)$	0.0005–0.0025 m²/mg	0.0005 m²/mg	5	Ahn et al., 1992; Reinart et al., 2004; Bricaud et al., 1983; Yang et al., 2011; Kirk, 2011; Jiang et al., 2020
$b^*_{btr}(550)$	0.005 - 0.025 m²/g	0.005 m²/g	5	Salem et al., 2017; Yang et al., 2011; Jiang et al., 2020
S_1	0.5–2.5	0.5	5	IOCCG, 2006; Reinart et al., 2004; Strömbeck and Pierson, 2001; Yang et al., 2011
S_2	0.5–2.5	0.5	5	IOCCG, 2006; Reinart et al., 2004; Strömbeck and Pierson, 2001; Yang et al., 2011
α	0.1–0.3 g/mg	0.1 g/mg	3	Östlund et al., 2001; Strömbeck and Pierson, 2001; Oyama et al., 2009; Xue et al., 2019

Table 3
The ranges and intervals of chlorophyll-a concentration, tripton concentration, and CDOM absorption coefficients at 440 nm used to generate Synthetic Dataset II.

Parameter	Range	Interval	Number
C_{chl}	0.01–0.1 mg/m³	0.01 mg/m³	63
	0.2–1 mg/m³	0.1 mg/m³	
	2–10 mg/m³	1 mg/m³	
	12–20 mg/m³	2 mg/m³	
	25–50 mg/m³	5 mg/m³	
	60–100 mg/m³	10 mg/m³	
	120–300 mg/m³	20 mg/m³	
	350–500 mg/m³	50 mg/m³	
	600–1000 mg/m³	100 mg/m³	
C_{tr}	0.01–0.1 g/m³	0.01 g/m³	63
	0.2–1 g/m³	0.1 g/m³	
	2–10 g/m³	1 g/m³	
	12–20 g/m³	2 g/m³	
	25–50 g/m³	5 g/m³	
	60–100 g/m³	10 g/m³	
	120–300 g/m³	20 g/m³	
	350–500 g/m³	50 g/m³	
	600–1000 g/m³	100 g/m³	
$a_{CDOM}(440)$	0.01–0.1 m⁻¹	0.01 m⁻¹	23
	0.2–1 m⁻¹	0.1 m⁻¹	
	2–5 m⁻¹	1 m⁻¹	

Table 4
The ranges and numbers of chlorophyll-a concentration, tripton concentration, and CDOM absorption coefficients at 440 nm to generate Synthetic Dataset III.

	C_{chl} (mg/m³)	C_{tr} (g/m³)	$a_{CDOM}(440)$ (m⁻¹)	Number of R_{rs} – TSS pairs
Range 1	0.01–0.1	0.01–0.1	0.01–0.05	200
Range 2	0.1–1	0.1–1	0.01–0.05	200
Range 3	1–10	1–10	0.05–0.1	200
Range 4	10–100	10–100	0.1–1	200
Range 5	100–1000	100–1000	1–5	200
Total	0.01–1000	0.01–1000	0.01–5	1000

g., Lee et al., 2002; IOCCG, 2006; Vaillancourt et al., 2004 for b^*_{bph}; and Giardino et al., 2007; Yang et al., 2011; Salem et al., 2017 for b^*_{btr}). Therefore, b^*_{bph} and b^*_{btr} are expressed as:

$$b^*_{bph}(\lambda) = b^*_{bph}(550) \cdot \left(\frac{\lambda}{550}\right)^{-S_1} \tag{2}$$

$$b^*_{btr}(\lambda) = b^*_{btr}(550) \cdot \left(\frac{\lambda}{550}\right)^{-S_2} \tag{3}$$

where $b^*_{bph}(550)$ is the mass-specific backscattering coefficient of phytoplankton at 550 nm, and $b^*_{btr}(550)$ is the mass-specific backscattering coefficient of tripton at 550 nm. S_1 and S_2 are the slopes of specific backscattering coefficient spectra for phytoplankton and tripton, respectively.

TSS concentration can be simulated based on tripton and Chl-a concentrations (Oyama et al., 2009; Xue et al., 2019):

$$TSS = \alpha \cdot C_{chl} + C_{tr} \tag{4}$$

where α is the fraction of phytoplanktonic suspended solids to Chl-a with a unit of g/mg (or mg/μg). Note, the "g/mg" was only used for unit conversion of α C_{chl}.

Table 2 shows the variation ranges, intervals, and references for all input parameters used to generate Synthetic Dataset I. In total, we generated 1,171,875 TSS-b_{bp} pairs.

Synthetic Datasets II and III include R_{rs} spectra and their corresponding TSS concentrations. The R_{rs} spectra were generated using a bio-optical model proposed by Gordon et al. (1988) and Lee et al. (2002) with assumptions of a nadir viewing angle and optically deep waters. The bio-optical model uses Chl-a concentration (C_{chl}), tripton concentration (C_{tr}), and the CDOM absorption coefficient at 440 nm

($a_{CDOM}(440)$), as well as the corresponding specific inherent optical properties (SIOPs) as input to first simulate the total absorption coefficient (a) and the total backscattering coefficient (b_b), which are then used to generate R_{rs} spectra from the simulated a and b_b values. The corresponding TSS concentrations were generated using Eq. (4) with an α value of 0.12 g/mg (Oyama et al., 2009). The SIOPs were sampled from Lake Kasumigaura, Japan on May 11, 2018. The absorption coefficients of phytoplankton and tripton, were obtained using the quantitative filter technique (Mitchell, 1990). The absorption coefficient of CDOM was measured using a spectrophotometer (UV-3100, Shimazu, Kyoto, Japan) with a 10 cm quartz cuvette to the filtered samples (filtered out by Whatman GF/F filter with a pore size of 0.7 μm). The backscattering coefficients of phytoplankton and tripton were obtained according to the method reported by Yang et al. (2011), in which a power-law function assumption for b^*_{btr} was used. More details on the simulation can be found in Jiang et al. (2020).

Table 3 shows the variation ranges and intervals of C_{chl}, C_{tr}, and $a_{CDOM}(440)$, which were used to generate Synthetic Dataset II. In all, we generated 91,287 synthetic data records, which include a, b_b, R_{rs} and the corresponding TSS values.

For Synthetic Dataset III, we first set five ranges for C_{chl}, C_{tr}, and $a_{CDOM}(440)$), respectively (Table 4). We then randomly selected 200 sets of C_{chl}, C_{tr}, and $a_{CDOM}(440)$ values to generate 200 R_{rs} and corresponding TSS pairs for each range. In all, we obtained 1000 R_{rs} and corresponding TSS pairs with C_{chl} values in the range of 0.01–1000 mg/

Table 5
Satellite matchups used for validation in this study.

Lake	Number of matchups	Image date	Sensor
Kasumigaura	81	2004/07/07–2020/03/11 (16 scenes)	MERIS, OLCI
Suwa	65	2006/04/03–2020/06/17 (65 scenes)	MERIS, OLCI
Akan	2	2019/08/27	OLCI
Taihu	1	2007/01/07	MERIS
Vieux Desert, WI	3	2016/06/28	OLCI
Winnebago, WI	5	2016/09/02	OLCI
Poygan, WI	5	2018/07/23, 2018/08/23, 2018/09/11	OLCI
Winneconne, WI	4	2018/07/23, 2018/08/23, 2018/09/11, 2018/10/24	OLCI
Green Bay of Lake Michigan, WI	4	2019/06/06, 2019/07/24	OLCI
Total	170		

Table 6
The median values of $1/b^{*}_{bp}$ obtained from Synthetic Dataset I.

Wavelength (nm)	$1/b^{*}_{bp}$ (g/m^2)	Wavelength (nm)	$1/b^{*}_{bp}$ (g/m^2)
413	56.306	681	118.147
443	61.843	709	126.342
490	74.906	754	137.665
510	81.633	761	139.451
560	94.607	779	142.816
620	106.180	865	166.168
665	114.012		

m^3, C_{tr} values in the range of 0.01–1000 g/m^3, and $a_{CDOM}(440)$ values in the range of 0.01–5 m^{-1}.

2.3. Satellite data collection and processing

MERIS and OLCI Level-1 data were used in this study because of their better spatial (300 × 300 m) and spectral (15 bands for MERIS and 21 bands for OLCI) characteristics than other ocean-colour sensors like MODIS. MERIS and OLCI images over three Japanese lakes (Lakes Kasumigaura, Suwa, and Akan), one Chinese lake (Lake Taihu), and five North American lakes (Lac Vieux Desert, Lakes Winnebago, Poygan, and Winneconne and Green Bay of Lake Michigan) were obtained from the European Space Agency (ESA, https://merisfrs-merci-ds.eo.esa.int). Atmospheric correction was done using the Case-2 Regional Processor in BEAM 5.0 for MERIS images, and using the C2RCC Processor in SNAP 7.0 for OLCI images. Clouds and cloud shadows were identified for both MERIS and OLCI images using the IdePix module in SNAP. Finally, the pixels with clouds, cloud shadows, cloud buffers, and failed atmospheric correction were masked out for all MERIS and OLCI images using the mask bands from IdePix.

The average of TSS values derived within a 3 by 3-pixel area was calculated and compared with the corresponding *in situ*-measured TSS values obtained on the same day (*i.e.* matchups). In total, we compiled 170 matchups from Lakes Kasumigaura, Suwa, Akan, Taihu, Vieux Desert, Winnebago, Poygan, Winneconne and Green Bay of Lake Michigan for validating the TSS estimation method (Table 5). In addition, 175 and 174 MERIS images from 2003 to 2012, 498 and 358 OLCI images

from 2016 to 2020 were used for long-term TSS estimation in Lake Kasumigaura and Lake Suwa, respectively.

3. Model development

3.1. Building a widely applicable relationship between TSS and b_{bp}

In addition to Eq. (1), the b_{bp} can also be written as follows (Nechad et al., 2010):

$$b_{bp}(\lambda) = TSS \cdot b^{*}_{bp}(\lambda), \qquad (5)$$

where b^{*}_{bp} is the TSS-specific particulate backscattering coefficient and TSS is the concentration of total suspended solids. Thus, TSS can be calculated as:

$$TSS = \frac{1}{b^{*}_{bp}(\lambda)} \cdot b_{bp}(\lambda) \qquad (6)$$

Due to the difficulty of obtaining a large number of b^{*}_{bp} spectral values from various water types through field surveys, we used Synthetic Dataset I to determine a representative range of values of b^{*}_{bp} for a variety of water types. Fig. 3 illustrates the basic statistics associated with the Synthetic Dataset I. The black asterisks and the red lines with solid circles represent the mean and median values of b^{*}_{bp} at the central wavelengths of major MERIS bands, respectively. To avoid the influence from extreme cases in the simulation, we used the median value of b^{*}_{bp} to build a relationship between b_{bp} and TSS for each wavelength. Table 6 lists the median values of $1/b^{*}_{bp}$ obtained from Synthetic Dataset I, which were subsequently used in our TSS estimation method.

3.2. Estimating b_{bp} from R_{rs} based on semi-analytical models

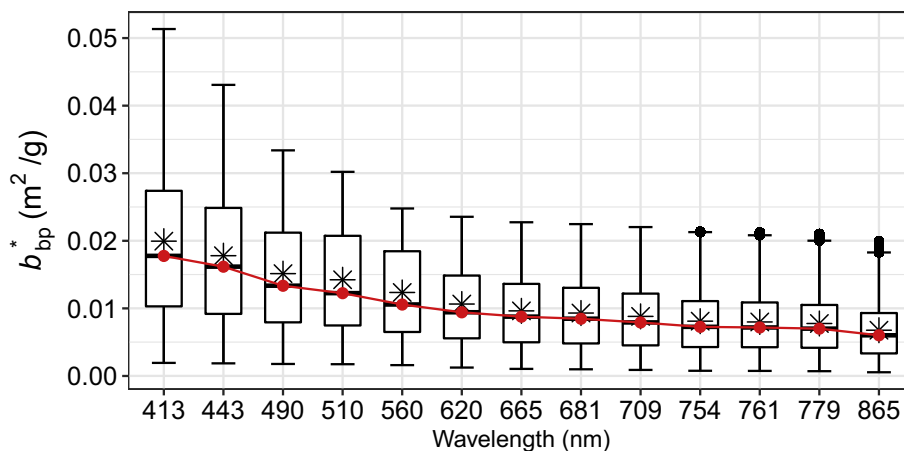According to Lee et al. (2002), b_{bp} can be semi-analytically estimated from the following equations:

Fig. 3. Statistics of the b^{*}_{bp} values from Synthetic Dataset I; the red solid circles represent the median value and the black asterisks represent the mean value. (For interpretation of the references to colour in this figure legend, the reader is referred to the web version of this article.)
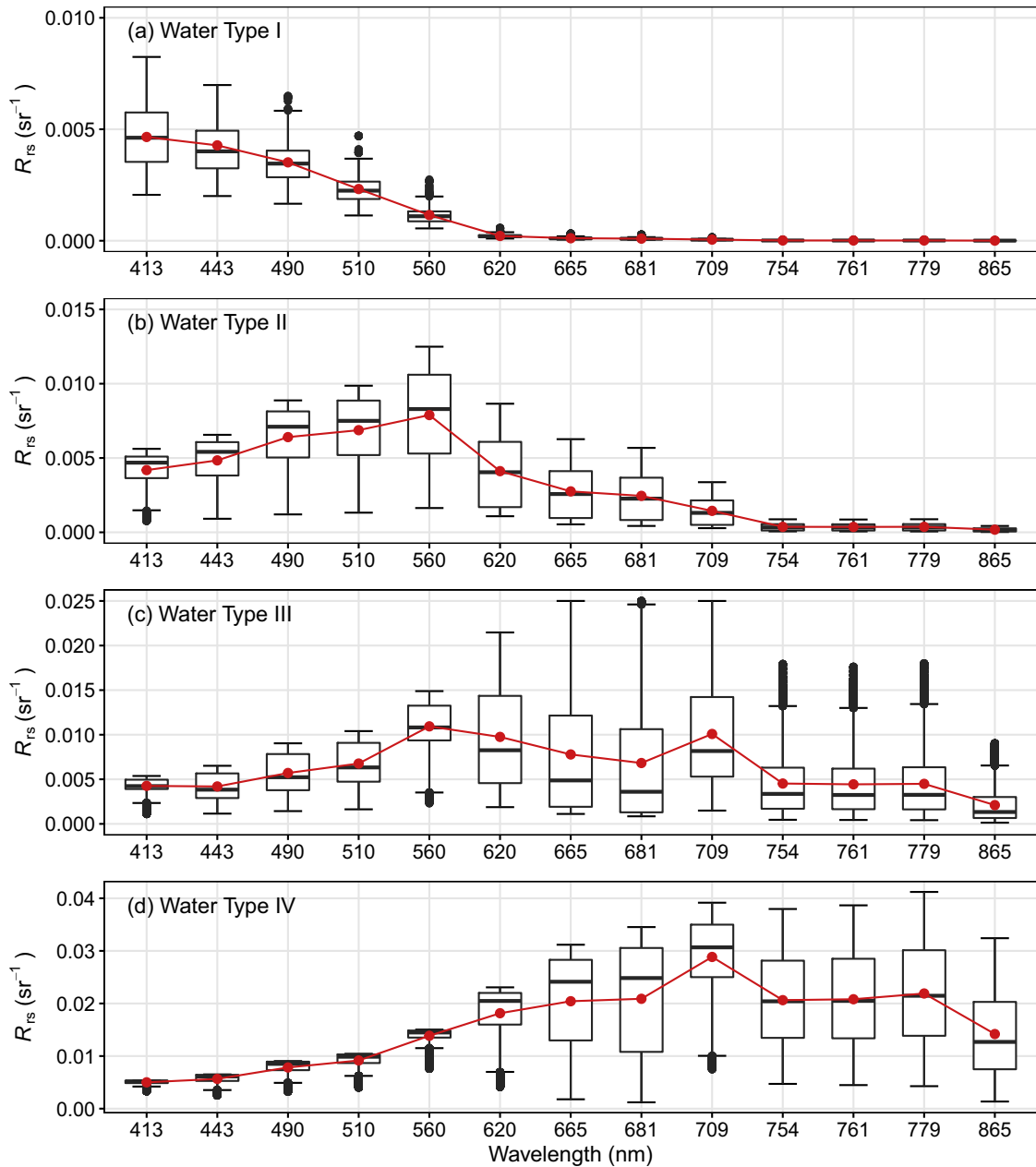
Fig. 4. Statistics of the R_{rs} spectral shapes for each water type obtained from Synthetic Dataset II. The red line with the solid circles represents the mean value of R_{rs} at each wavelength. (a) Type I waters, (b) Type II waters, (c) Type III waters, and (d) Type IV waters. (For interpretation of the references to colour in this figure legend, the reader is referred to the web version of this article.)

$$r_{rs}(\lambda) = R_{rs}(\lambda) / (0.52 + 1.7 R_{rs}(\lambda)), \tag{7}$$

$$u(\lambda) = \frac{-0.089 + \sqrt{0.089^2 + 4 \times 0.125 r_{rs}(\lambda)}}{2 \times 0.125}, \tag{8}$$

$$b_{bp}(\lambda) = \frac{u(\lambda) \times a(\lambda)}{1 - u(\lambda)} - b_{bw}(\lambda), \tag{9}$$

where a is the total absorption coefficient, b_{bw} is the backscattering coefficient of pure water (Zhang et al., 2009), R_{rs} is the remote-sensing reflectance just above the water surface, and r_{rs} is the remote-sensing reflectance just below the water surface.

There are two unknowns in Eq. (9) (*i.e.*, $a(\lambda)$ and $b_{bp}(\lambda)$). To solve the problem, Lee et al. (2002) suggested the use of a reference wavelength (λ_0), at which the absorption coefficient of pure water dominates the total absorption coefficient. Therefore, at the reference wavelength, an

unknown value of $a(\lambda_0)$ can be assumed to be equal to $a_w(\lambda_0)$ (*i.e.* $a(\lambda_0) \approx a_w(\lambda_0)$), and the corresponding unknown value of $b_{bp}(\lambda_0)$ can then be calculated using Eq. (9). In this study, we chose R_{rs} at different reference wavelength to estimate corresponding values of b_{bp} and then TSS for different water types. The reference wavelength selection is based on the following two conditions: (1) the assumption of $a(\lambda_0) \approx a_w(\lambda_0)$ is valid; and (2) the R_{rs} at the reference wavelength ($R_{rs}(\lambda_0)$) is sensitive to the variation of TSS values. Based on the absorption characteristics of pure water, the longer the wavelength, the easier it is to satisfy the first condition. However, if the wavelength is too long, the second condition may not be satisfied due to the very low R_{rs}.

Based on the above two conditions, we defined four water types (*i.e.*, clear waters, moderately turbid waters, highly turbid waters, and extremely turbid waters) and chose a reference wavelength for each water type. For clear waters (*e.g.*, open ocean, hereafter Type I), we
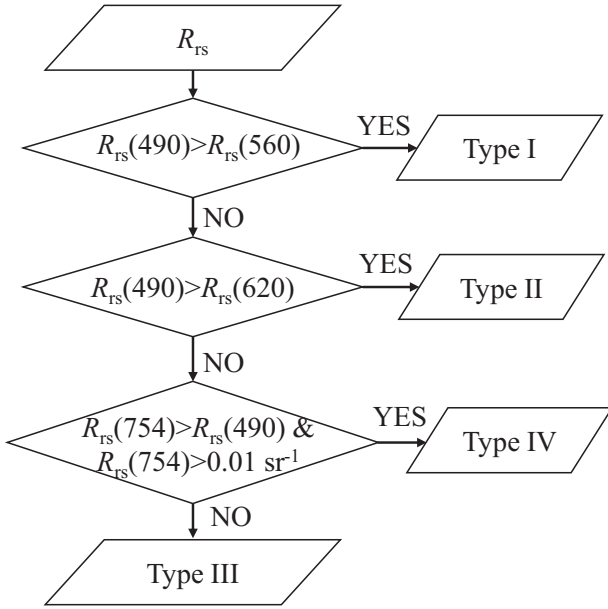
Fig. 5. Flowchart of water type classification algorithm proposed in this study.

chose 560 nm as the reference wavelength. An empirical equation was also used to further improve the estimation accuracy of $a(560)$ (Lee et al., 2002):

$$a(560) = a_w(560) + 10^{-1.146-1.366x-0.469x^2},$$ (10)

$$x = log\left(\frac{r_{rs}(443) + r_{rs}(490)}{r_{rs}(560) + 5\frac{r_{rs}(665)}{r_{rs}(490)}r_{rs}(665)}\right)$$ (11)

However, for moderately turbid waters (*e.g.*, coastal waters,

hereafter Type II), the $a(560) \approx a_w(560)$ assumption is no longer valid. In these waters, we used 665 nm as the reference wavelength. The a (665) can be estimated using the following semi-analytical equation (IOCCG, 2014):

$$a(665) = a_w(665) + 0.39 \cdot \left(\frac{R_{rs}(665)}{R_{rs}(443) + R_{rs}(490)}\right)^{1.14}$$ (12)

Note, empirical components in Eqs. (10−12) contribute relatively small errors in estimations of $a(560)$ and $a(665)$ based on the first condition (Lee et al., 2002; IOCCG, 2014).

For highly turbid waters (hereafter Type III), we chose 754 nm as the reference wavelength instead of 560 nm and 665 nm (Yang et al., 2013) for two reasons. First, as turbidity increases the particulate absorption coefficients increase dramatically at shorter wavelengths. In such cases, the assumption of $a \approx a_w$ is no longer valid at 560 and 665 nm, where the pure-water absorption coefficients are less than 0.43 m^{-1} (Pope and Fry, 1997). In contrast, the pure-water absorption coefficient at 754 nm reaches 2.87 m^{-1} (Kou et al., 1993), which is several times higher than those at 560 and 665 nm, and the assumption of $a(754) \approx a_w(754)$ therefore becomes valid. Second, $R_{rs}(754)$ is sensitive to TSS due to the increased particulate backscattering coefficient.

Similar to Type III waters, for extremely turbid waters (hereafter Type IV), the reference wavelength should be further shifted to longer wavelengths, for example, 865 nm, because $a_w(865)$ can reach 4.6 m^{-1} (Kou et al., 1993), and thus the assumption of $a(865) \approx a_w(865)$ is likely valid even in extremely turbid waters.

Following the estimation of $a(\lambda_0)$, $b_{bp}(\lambda_0)$ can be calculated from $R_{rs}(\lambda_0)$ using the semi-analytical relationships in Eqs. (7)–(9). As the assumption for $a(\lambda_0) \approx a_w(\lambda_0)$ is of central importance for accurate retrieval of $b_{bp}(\lambda_0)$, it is necessary to determine water types before the b_{bp} calculations.

3.3. Classifying water types

We used Synthetic Dataset II to determine the characteristic spectral shapes of R_{rs} for each of the four water types described above. To fulfill
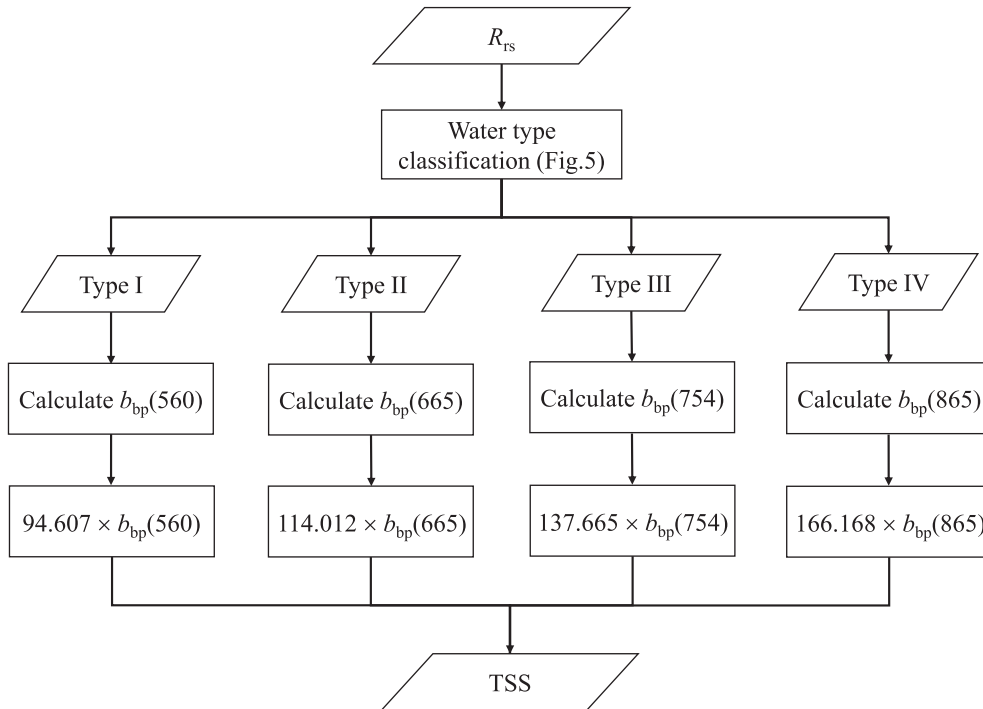

Fig. 6. Flowchart of the new method for TSS estimation proposed in this study. Water type classification is based on Fig. 5, and the coefficients for estimating TSS from b_{bp} are from Table 6.
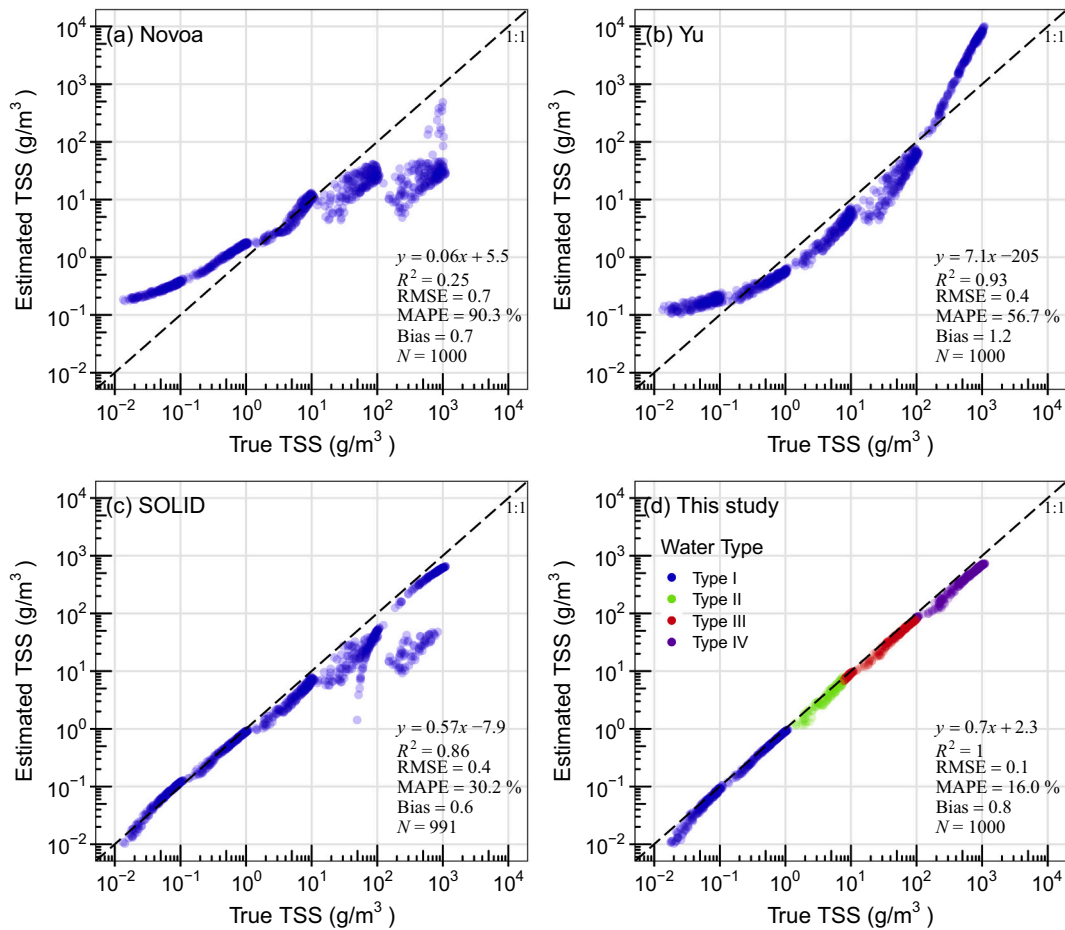
Fig. 7. Comparison of true and estimated TSS values. The estimated TSS values were obtained from the simulated R_{rs} in Synthetic Dataset III using different estimation methods. (a) using the method proposed by Novoa et al. (2017), (b) using the method proposed by Yu et al. (2019), (c) using the SOLID method proposed by Balasubramanian et al. (2020), and (d) using the new method proposed in this study.

the assumption of $a(\lambda_0) \approx a_w(\lambda_0)$, we set a threshold condition of $a_w(\lambda_0)/a(\lambda_0) > 0.8$ (*i.e.* the absorption coefficient of pure water accounts for more than 80% of the total absorption coefficient) for each water type. In addition, to exclude the influence of R_{rs} spectra from less turbid waters on the analyses of R_{rs} spectral shapes in more turbid waters, we selected R_{rs} spectra with TSS > 1 g/m^3 and $a_w(665)/a(665) > 0.8$ for analyzing the R_{rs} spectral shape of Type II waters, with TSS > 10 g/m^3 and $a_w(754)/a(754) > 0.8$ for analyzing the R_{rs} spectral shape of Type III waters, and with TSS > 100 g/m^3 and $a_w(865)/a(865) > 0.8$ for analyzing the R_{rs} spectral shape of Type IV waters. By applying the above criteria, we obtained the statistical R_{rs} spectral shape for each water type (Fig. 4).

From Fig. 4(a), it can be seen that the highest R_{rs} value is observed in the blue spectral region for Type I waters, and then shifts gradually from the blue to the red wavelengths. Therefore, a condition of $R_{rs}(490) > R_{rs}(560)$ can be used to identify Type I waters. For Type II waters, the R_{rs} value at a green wavelength becomes the highest one, but the R_{rs} value at the longer blue wavelength (490 nm) is still higher than that at the shorter red wavelength (620 nm) (Fig. 4(b)). Therefore, a condition of $R_{rs}(490) > R_{rs}(620)$ can be used sequentially to identify Type II waters. From Fig. 4(d), it can be seen that the highest R_{rs} value of Type IV waters is located at a NIR wavelength due to the stronger absorption at shorter wavelengths and stronger backscattering at longer wavelengths resulting from the high concentrations of particles (or algal materials) in the water bodies. In addition, to accommodate the extreme turbidity in Type IV waters, a condition of $R_{rs}(754) > R_{rs}(490)$ with $R_{rs}(754) > 0.01$ sr^{-1} is suggested to identify Type IV waters in this study. After identifying Type I, Type II, and Type IV waters, the remaining waters are classified as

Type III. The flowchart of water type classification is shown in Fig. 5. In comparison to previous studies (*e.g.* Novoa et al., 2017; Balasubramanian et al., 2020), the new water type classification method has fulfilled the assumption of $a(\lambda_0) \approx a_w(\lambda_0)$, which can lead to a more accurate $b_{bp}(\lambda_0)$ estimation (see Section 3.2).

Fig. 6 summarizes the proposed method for estimating TSS from a $R_{rs}(\lambda)$ spectrum. It includes three main steps: (1) water type classification (Fig. 5); (2) b_{bp} calculation at the appropriate reference wavelength (λ_0) according to the determined water type; and (3) TSS estimation using the corresponding relationship between TSS and b_{bp} (Table 6).

3.4. Accuracy assessment

We used the root mean square error (RMSE) in a log10 unit, the median absolute percentage error (MAPE), and bias to evaluate the performance of the proposed method. The equations are as follows:

$$\text{RMSE} = \sqrt{\frac{\sum_{i=1}^{N}\left[log_{10}\left(X_{estimated,i}\right) - log_{10}\left(X_{measured,i}\right)\right]^2}{N}} \tag{13}$$

$$\text{MAPE} = \text{median}\left(\left|\frac{X_{estimated,i} - X_{measured,i}}{X_{measured,i}}\right| \cdot 100\%\right), i = 1, \ldots, N \tag{14}$$

$$\text{Bias} = 10^Y, Y = \frac{\sum_{i=1}^{N}\left[log_{10}\left(X_{estimated,i}\right) - log_{10}\left(X_{measured,i}\right)\right]}{N} \tag{15}$$

Table 7
Performance statistics obtained from Synthetic Dataset III for four methods by water type (and all data pooled). Values in bold print with blue background represent the smallest values for RMSE and MAPE, the values closest to 1 for Slope, R^2, and Bias, and the values closest to 0 for Intercept.

Method	Water type	Slope	Intercept	R^2	RMSE	MAPE(%)	Bias	N
Novoa	Type I	1.58	0.21	0.99	0.57	242.56	3.28	400
	Type II	**1.06**	-0.49	0.81	**0.09**	**14.04**	**0.93**	117
	Type III	0.23	7.26	0.63	0.40	54.61	0.50	266
	Type IV	0.06	**1.88**	0.10	1.30	95.61	0.05	217
	All	0.06	5.48	0.25	0.73	90.31	0.71	1000
Yu	Type I	0.44	0.14	0.96	0.38	54.18	1.45	400
	Type II	0.52	-0.17	0.84	0.34	52.48	0.47	117
	Type III	0.59	-3.02	0.85	0.36	50.06	0.47	266
	Type IV	9.70	-2048.49	0.95	0.67	378.87	3.71	217
	All	7.13	-204.73	0.93	0.45	56.74	**1.16**	1000
SOLID	Type I	0.89	0.02	**1.00**	**0.06**	12.20	**1.01**	400
	Type II	0.64	**-0.03**	**0.93**	0.21	36.28	0.63	117
	Type III	0.37	1.69	0.82	0.40	55.21	0.44	257
	Type IV	**0.71**	-105.91	0.74	0.70	38.10	0.31	217
	All	0.57	-7.93	0.86	0.39	30.23	0.60	991
This study	Type I	**0.91**	**0.00**	**1.00**	0.12	**10.75**	0.84	400
	Type II	**0.94**	-0.34	**0.93**	**0.09**	14.77	0.84	117
	Type III	**0.81**	**0.57**	**1.00**	**0.08**	**15.44**	**0.84**	266
	Type IV	0.69	10.35	**0.99**	**0.15**	**29.72**	**0.71**	217
	All	**0.70**	**2.31**	**1.00**	**0.11**	**15.97**	0.81	1000

where $X_{\text{estimated}}$ is the estimated TSS value, X_{measured} is the corresponding *in situ*-measured TSS value, and N is the number of data pairs. The regression results between estimated and *in situ*-measured TSS values were also used to help assess algorithm performance (*e.g.*, slope, intercept, and R^2).

In addition, we compared the performance of the proposed TSS estimation method with those of three recently published TSS estimation methods, which were proposed by Novoa et al. (2017), Yu et al. (2019) and Balasubramanian et al. (2020; *i.e.*, SOLID: Statistical, inherent Optical property-based, and muLti-conditional Inversion proceDure).

4. Results

4.1. Validation using synthetic dataset III

Fig. 7 compares "true TSS values" and estimated TSS values from Synthetic Dataset III using three existing methods in addition to the new method proposed in this study. The new method proposed in this study accurately estimates TSS in all four water types with an MAPE of 16.0% and RMSE of 0.1 in log TSS units (Fig. 7d). The TSS values estimated through the new method show a very high correlation with the true TSS values, but with a slight underestimation ($R^2 = 1$, Bias = 0.8, and slope = 0.7). In contrast, the method proposed by Novoa et al. (2017) yields
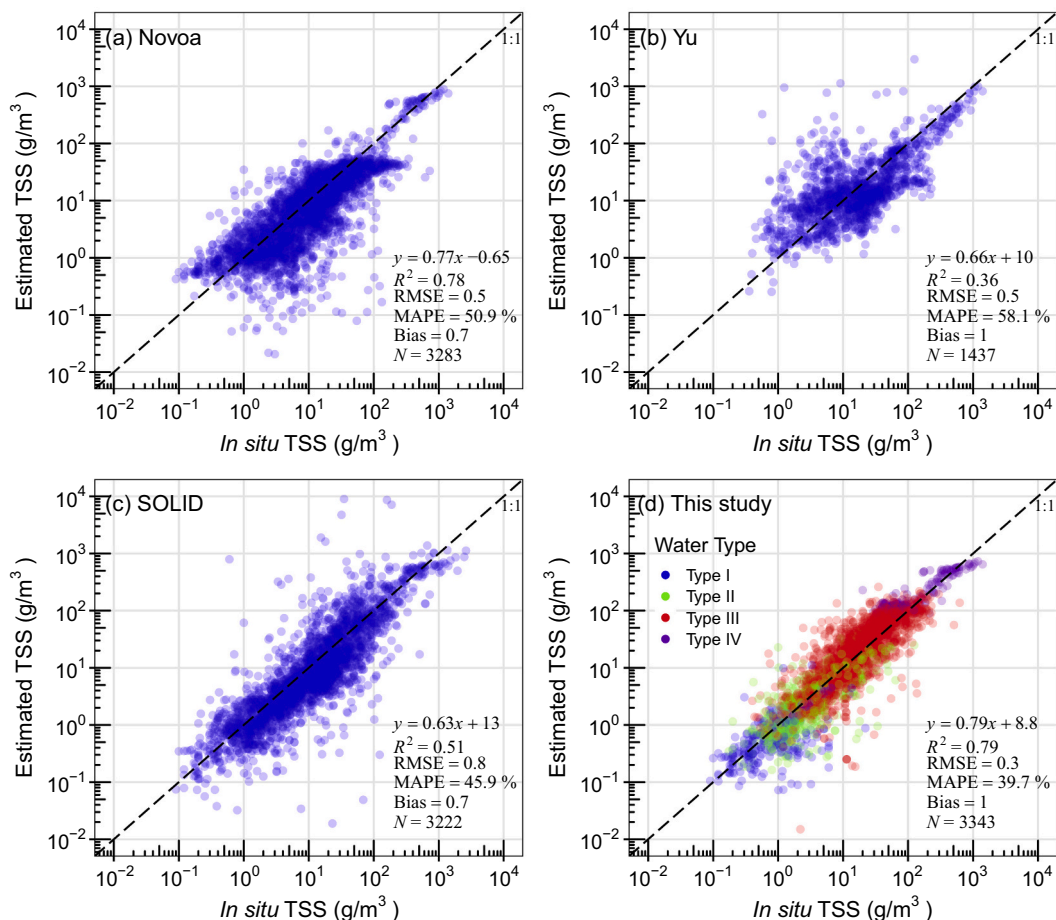
Fig. 8. Comparison of *in situ*-measured and estimated TSS values. The estimated TSS values were obtained from *in situ*-measured R_{rs} using different estimation methods. (a) using the method proposed by Novoa et al. (2017), (b) using the method proposed by Yu et al. (2019) (left out two outliers), (c) using the SOLID method proposed by Balasubramanian et al. (2020) (left out six outliers), and (d) using the new method proposed in this study.

overestimations for low TSS and large underestimations for high TSS values (RMSE in log10 unit = 0.7, MAPE = 90.3%, Fig. 7(a)); the method proposed by Yu et al. (2019) produces large overestimations for low and high TSS, and underestimations for moderate TSS (RMSE in log10 unit = 0.4, MAPE = 56.7%, Fig. 7(b)); and the SOLID method shows a good performance for low TSS, but produces large underestimations for TSS values larger than 10 g/m³ (RMSE in log10 unit = 0.4, MAPE = 30.2%, Fig. 7(c)).

Table 7 contains the performance statistics for each water type for the four methods. Although several assessment metrics for the existing methods show slightly better performance than the new method, the new method outperformed them in most cases (see values in bold print with blue background in Table 7). It should be noted that the number of data points from the SOLID method is less than 1000 because nine negative TSS estimations were removed.

4.2. Validation using the In Situ dataset

Fig. 8 compares *in situ*-measured and estimated TSS values. TSS concentrations were estimated from *in situ*-measured R_{rs} spectra using the three existing methods and the new method proposed in the present study. It should be noted that the number of available data points for each method is different. In total, we compiled 3421 R_{rs}-TSS data pairs from various waters. However, since some *in situ*-measured R_{rs} spectra do not include wavelengths longer than 800 nm, the new method is unable to estimate TSS if the corresponding waters were classified as Type IV. Therefore, the results in Fig. 8d only include 3343 data pairs. Similarly, as the method proposed by Novoa et al. (2017) needs R_{rs} at

862 nm for TSS estimation when $\rho_w(671) > 0.08$, 3283 data pairs remained. For the method proposed by Yu et al. (2019), since the method always needs the R_{rs} at 862 nm in the TSS estimation, only 1439 data pairs were available from the whole *In Situ* Dataset. We also omitted two outliers with TSS estimations larger than 4000 g/m³ (Fig. 8b). Although the SOLID method does not need R_{rs} at wavelengths longer than 800 nm, only 3222 data pairs are shown in Fig. 8c because 193 negative TSS estimations and six outliers with TSS estimations larger than 4000 g/m³ were removed.

Overall, the new method proposed in this study presents the highest accuracy and the smallest MAPE value of 39.7% (45.9%–58.1% for other methods) and RMSE value of 0.3 in log10 TSS units (0.5–0.8 for other methods). In addition, the new method also had the highest R^2 value (0.79) and no bias (value of 1). Thus, the new method can provide accurate TSS retrievals across Type I to Type IV waters (Fig. 8d).

Table 8 lists the performance statistics obtained from the *In Situ* Dataset for each water type and the four methods. RMSE values were lowest using the new method for all four water types. Values of MAPE for the new method were also the lowest, except for Type IV waters (39.23%). For Type IV waters, lower values of MAPE (34.12%), but a higher RMSE (0.30) value were found for the method proposed by Yu et al. (2019) as compared to the new method.

4.3. Validation using satellite matchups

Fig. 9 shows the comparison between *in situ*-measured and estimated TSS concentrations from MERIS and OLCI images using the new method (170 matchups). The *in situ*-measured TSS values ranged from 1.2 g/m³

Table 8
Performance statistics obtained from the *In Situ* Dataset for four methods by water type (and all data pooled). Values in bold print with blue background represent the smallest values for RMSE and MAPE, the values closest to 1 for Slope, R^2, and Bias, and the values closest to 0 for Intercept.

Method	Water type	Slope	Intercept	R^2	RMSE	MAPE(%)	Bias	N
Novoa	Type I	**0.40**	1.22	**0.13**	0.42	81.61	1.50	302
	Type II	0.54	2.88	**0.38**	0.34	43.84	**0.96**	814
	Type III	0.38	**7.02**	0.39	0.52	51.60	0.56	1991
	Type IV	**0.80**	**2.87**	0.74	0.47	45.59	0.55	176
	All	0.77	**-0.65**	0.78	0.47	50.92	0.70	3283
Yu	Type I	-3.06	62.12	0.00	0.99	219.35	3.26	28
	Type II	**0.89**	13.94	0.00	0.59	73.94	1.65	196
	Type III	0.42	11.84	0.02	0.48	59.74	0.89	1061
	Type IV	0.63	40.60	0.65	0.30	**34.12**	**0.80**	152
	All	0.66	10.18	0.36	0.50	58.07	0.98	1437
SOLID	Type I	0.19	0.66	**0.13**	0.43	52.97	**0.74**	302
	Type II	0.52	**1.76**	0.19	0.36	39.24	0.71	815
	Type III	**0.72**	10.78	0.11	0.85	48.98	0.68	1876
	Type IV	0.51	108.41	0.55	1.87	40.49	0.53	229
	All	0.63	13.12	0.51	0.85	45.86	0.68	3222
This study	Type I	0.19	**0.61**	0.11	**0.41**	**42.52**	0.69	301
	Type II	0.41	2.53	**0.38**	**0.31**	**37.78**	0.84	815
	Type III	0.60	14.08	**0.47**	**0.32**	**40.00**	**1.09**	2074
	Type IV	0.63	110.44	**0.78**	**0.27**	39.23	1.41	153
	All	**0.79**	8.79	**0.79**	**0.33**	**39.66**	**1.00**	3343

to 88.7 g/m^3, which cover Type II (Lake Akan) and Type III (others) waters. TSS values were accurately estimated in most cases with a MAPE value of 35.5%, RMSE value of 0.4, and a bias value of 0.8. In particular, the matchups obtained from Lake Kasumigaura, Japan ($N = 81$) showed good agreement with the MAPE values of 28.8%. For the matchups obtained from Lake Suwa, Japan ($N = 65$), the new method also showed good performance except for seven matchups with *in situ* TSS concentrations lower than 10 g/m^3. If these seven matchups are excluded, the MAPE value for Lake Suwa is reduced from 43.3% to 35.6%. Generally, large underestimations were found in areas where *in situ* TSS < 10 g/m^3 (*e.g.* in Lake Akan, Lac Vieux Desert, and several matchups in Lake Suwa). This is probably due to an imperfect atmospheric correction of

the satellite images (see discussion in Section 5.2).

4.4. Long-term TSS time-series in Lake Kasumigaura and Lake Suwa, Japan

Figs. 10 and 11 show the comparison of *in situ*-measured and satellite-estimated TSS concentrations (MERIS and OLCI) in Lake Kasumigaura and Lake Suwa, respectively, for an 18-year period (2003−2020). In Lake Kasumigaura, 207 *in situ* TSS values (monthly data) were measured for each site during the study period. In contrast, we obtained more than 431 satellite-derived TSS values (maximum number of 554 at the lake center) for each site in the same period.
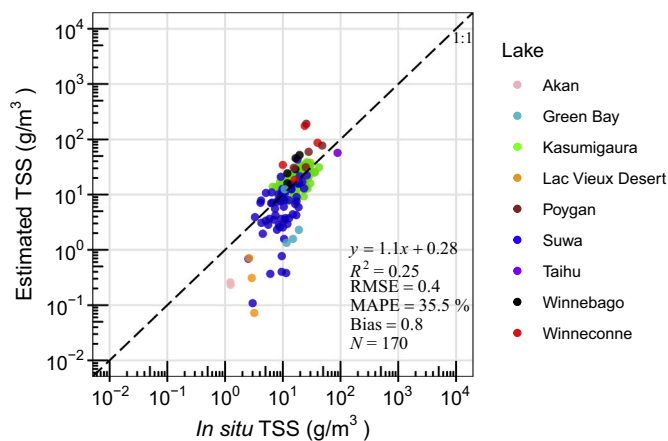
Fig. 9. Comparison of *in situ*-measured TSS and estimated TSS from MERIS/OLCI images using the new method.

During the period of 2016–2020, there were 8.5 to 10.9 times more OLCI retrievals than *in situ* TSS measurements (Fig. 10). In Lake Suwa, 715 *in situ* TSS values (almost weekly data) were measured from 2003 to 2020, whereas we obtained 174 MERIS-derived TSS values from 2003 to 2012, and 358 OLCI-derived TSS values from 2016 to 2020. The observation frequency of OLCI is still higher than that of field surveys during 2016–2020 (Fig. 11).

Visually, the satellite-derived TSS values agree well with the *in situ*-measured TSS values (Figs. 10 and 11). In Lake Kasumigaura, both *in situ*-measured and satellite-derived TSS values show comparable decreasing trends from 2003 to 2012 (slope < 0 and *p* value<0.01 based on a linear regression analysis) but higher values from late 2019 to early 2020 (Fig. 10). In Lake Suwa, *in situ*-measured and satellite-derived TSS values show decreasing trends from 2003 to 2020 (Fig. 11, slope < 0 and p value<0.05 based on a linear regression analysis). During the period of 2016–2020, as the high observation frequency of the OLCI, a clear seasonal variation of TSS can be seen in both lakes. For example, at sites 3 and 7 in Lake Kasumigaura, OLCI-derived TSS concentrations are higher in summer and lower in winter between 2016 and 2020, which agrees well with the pattern observed with *in situ*-measured TSS data (Fig. 10a and c). It is also notable that several extremely high TSS events were observed from OLCI data (green dots) but were not captured by the field surveys between 2016 and 2020. In contrast, during 2003–2012, peaks in TSS concentration were observed in *in situ* data (blue dots) but not in MERIS data. These very high TSS values resulted from resuspension by typhoons (also see Figs. 13j – 13 l), as Lake Kasumigaura and Lake Suwa are both shallow.

4.5. Showcase of TSS spatial distribution maps

The new TSS estimation method was applied to map spatial distributions of TSS from OLCI images over the three longest river estuaries (Nile River, 2020/05/20; Amazon River, 2019/08/24; Yangtze River, 2018/04/08) and four lakes in Africa and Asia (Lake Victoria, 2016/08/17; Lake Turkana, 2020/03/13; Lake Qinghai, 2020/06/29; and Lake Kasumigaura, 2019/10/13).

Fig. 12 illustrates the standard false colour OLCI images (R:G:B = 17:8:6), water type classification maps, and TSS distribution maps for the three river estuaries. It can be seen that the Nile River Estuary lacked Type III (highly turbid) and Type IV (extremely turbid) waters in contrast to the Amazon and Yangtze River Estuaries (Fig. 12b, e, h). In the Amazon and Yangtze River Estuaries, we can clearly observe that water types change from Type IV to Type I from the river mouths to the open ocean. In the Amazon River Estuary, Type IV waters extend ~110 km offshore. As expected, the TSS distributions in the three estuaries showed a gradual decrease in TSS concentrations from the river mouths

into the open ocean (Fig. 12c, f, i).

Prominent spatial heterogeneity of the TSS distribution was also observed in the four example lakes (Fig. 13). Different from the spatial distribution patterns in the estuaries in Fig. 12, the TSS values in Lake Victoria and Lake Qinghai gradually decreased from the shoreline to the center of the lakes (Fig. 13c, f), whereas they gradually decreased from the north to the south in Lake Turkana (Fig. 13i). Type IV waters and very high TSS concentrations (with a lake averaged value of 86 g/m^3) were temporarily observed in the central and western parts of Lake Kasumigaura due to resuspension by Typhoon Hagibis, which made landfall in Japan on October 12, 2019 (Fig. 13k, l).

5. Discussion

5.1. Applicability of the new TSS estimation method

In this study, we proposed a widely applicable method for estimating TSS from remote sensing data in clear to extremely turbid waters. To this end, all development procedures were based on semi-analytical models and synthetic datasets with wide ranges of inherent optical properties. For example, to build a widely applicable relationship between b_{bp} and TSS, we generated a large dataset (Synthetic Dataset I; $N = 1,171,875$), in which the magnitude and the spectral shape of b_{bp} as well as TSS concentrations varied widely. Therefore, the adoption of the median b^*_{bp} from Synthetic Dataset I can commonly represent most water bodies. To allow us to accurately estimate b_{bp} from R_{rs} using the semi-analytical model in various waters, we employed four reference wavelengths (560, 665, 754, and 865 nm) and switched between them depending on four water types. The adoption of multiple reference wavelengths has two advantages: (1) the assumption of $a \approx a_w$ is always fulfilled, and (2) a TSS-sensitive wavelength (band) is chosen automatically to match the expected turbidity levels of the water. Moreover, to classify water types accurately, we used another large synthetic dataset (Synthetic Dataset II; $N = 91,287$), to develop the classification algorithm.

The validation results obtained from 1000 independently simulated and 3421 globally distributed *in situ* R_{rs}-TSS data pairs, as well as the satellite-derived long-term TSS time-series in two Japanese lakes, collectively indicate that our proposed TSS estimation method can be successfully used in a wide range of waters without needing to vary parameter values (Figs. 7d, 8d, 10, and 11). However, from the simulations shown in Fig. 3, we demonstrate that the value of b^*_{bp} varied at each wavelength due to variable SIOPs. Therefore, one should be cautious when applying the median b^*_{bp} value to extreme cases, even though these extreme cases are probably rare in the natural world. For example, we found slight overestimations in Lake Erie ($N = 328$, MAPE = 49%, RMSE = 0.3, and Bias = 1.4) using the proposed TSS estimation method. Binding et al. (2019) reported that cyanobacteria occurrences in Lake Erie are associated with higher b_{bp} values compared to other phytoplankton species due to their different cell morphology. Therefore, the value of b^*_{bp} in Lake Erie was slightly larger than the median b^*_{bp} used in this study. If we use upper quartile b^*_{bp} values instead of the median b^*_{bp} values for Lake Erie, the overestimation is improved (MAPE = 40%, RMSE = 0.3, Bias = 0.9). Consequently, although we have shown that the proposed median b^*_{bp} values can be widely used in various waters, if actual b^*_{bp} values are available in a water body, users can simply replace the proposed median b^*_{bp} values with their own measured b^*_{bp} values to obtain more accurate regionally-tuned estimates of TSS concentration.

5.2. Influence of R_{rs} accuracy on TSS estimation

Since the proposed method uses a single band to estimate TSS values from R_{rs}, the accuracy of R_{rs} will strongly influence the accuracy of TSS estimations. For example, several previous studies found that the R_{rs} spectra measured using the above-water approach frequently suffer
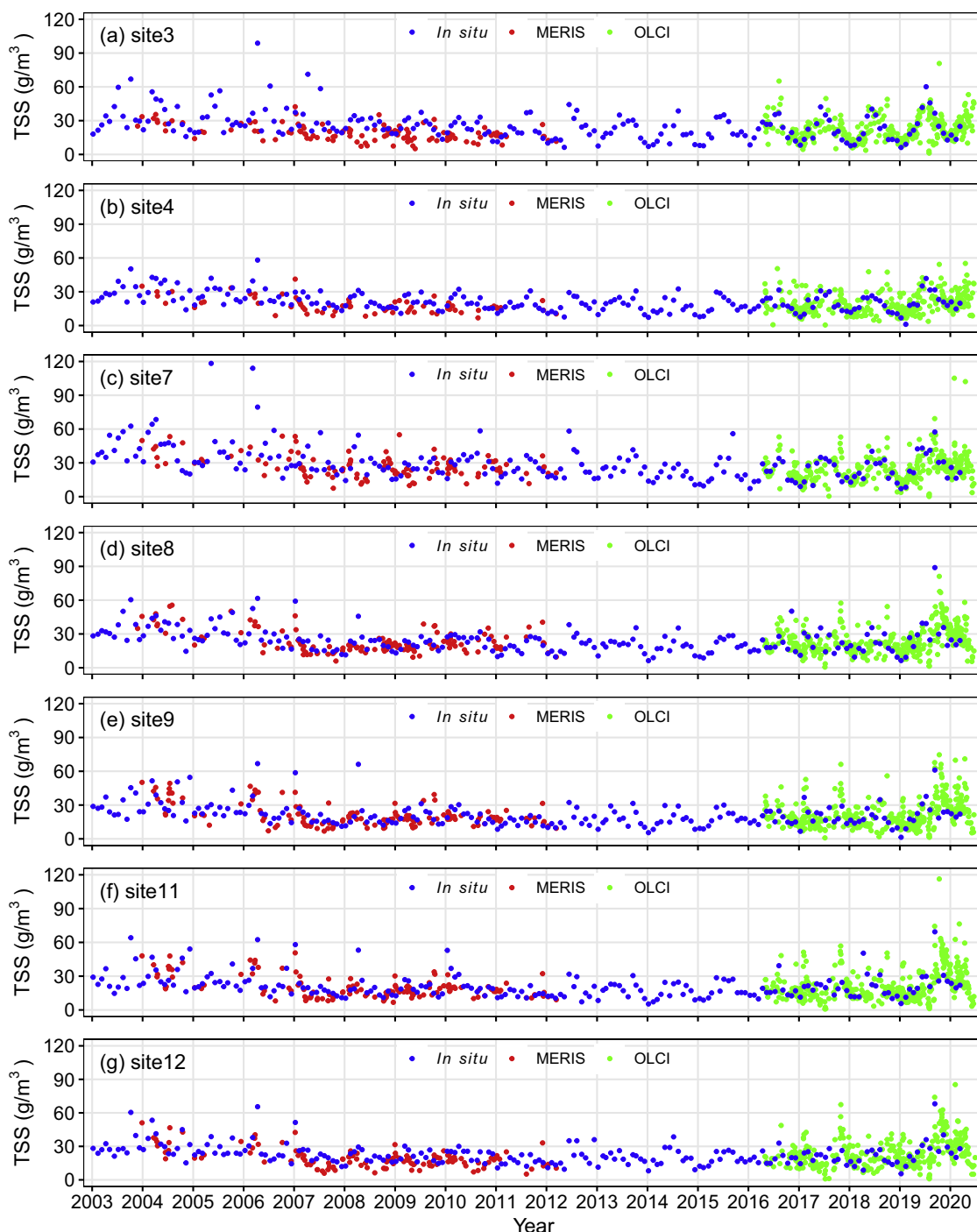
Fig. 10. Long-term TSS time-series at seven sites in Lake Kasumigaura shown in Fig. 1. Blue dots represent *in situ*-measured TSS, red dots represent TSS estimated from MERIS images, and green dots represent TSS estimated from OLCI images. (For interpretation of the references to colour in this figure legend, the reader is referred to the web version of this article.)

from the effects of residual reflected skylight (Δ) (Ruddick et al., 2005; Lee et al., 2010; Kutser et al., 2013; Groetsch et al., 2017; Jiang et al., 2020). In this study, we compiled 1110 R_{rs} spectra measured using the above-water approach. We used Jiang et al. (2020) or Ruddick et al. (2005) methods to correct the Δ effects for 973 R_{rs} spectra. The remaining 137 R_{rs} spectra did not require this correction because skylight effects were already corrected for by the data provider (Knaeps et al., 2018). Without the corrections, the MAPE, RSME, and Bias associated with TSS retrievals would have increased from 39.7% to 63.4%, 0.3 to 0.4, and 1.1 to 1.6, respectively (Fig. 14).

Atmospheric correction remains a challenge over coastal and inland waters for obtaining accurate R_{rs} and thus accurate TSS estimations from satellite images (Balasubramanian et al., 2020). In this study, we used the Case 2 Regional Processor implemented in BEAM 5.0 and SNAP 7.0 to carry out atmospheric correction for MERIS and OLCI images, and observed larger underestimations in TSS when the *in situ*-measured TSS values were lower than 10 g/m^3 (Fig. 9). It is likely that inaccurate atmospheric corrections caused differences in the magnitude and shape of the atmospherically corrected R_{rs} spectra relative to those obtained with field surveys. For example, the shapes of OLCI atmospherically corrected
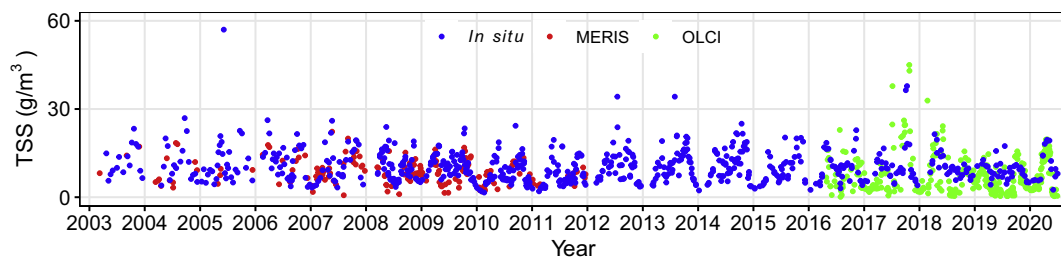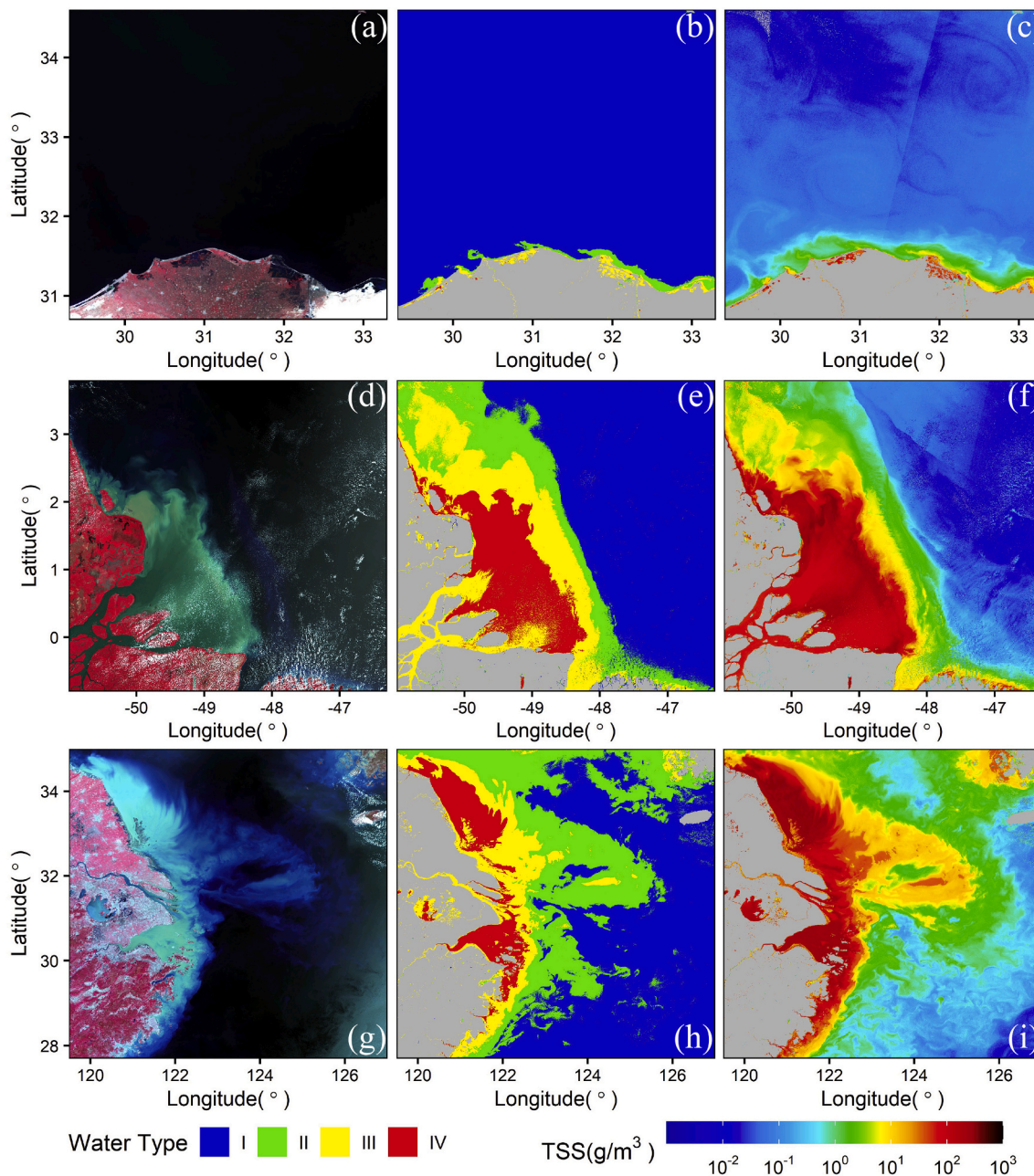
Fig. 11. Long-term TSS time-series at the center of Lake Suwa. Blue dots represent *in situ*-measured TSS, red dots represent TSS estimated from MERIS images, and green dots represent TSS estimated from OLCI images. (For interpretation of the references to colour in this figure legend, the reader is referred to the web version of this article.)

Fig. 12. Showcase maps for the three longest river estuaries, showing the RGB OLCI image, the water type classification map, and the estimated TSS values for: (a)-(c) the Nile River Estuary (May 20, 2020), (d)-(f) the Amazon River Estuary (Aug. 24, 2019), and (g)-(i) the Yangtze River Estuary (Apr. 8, 2018).
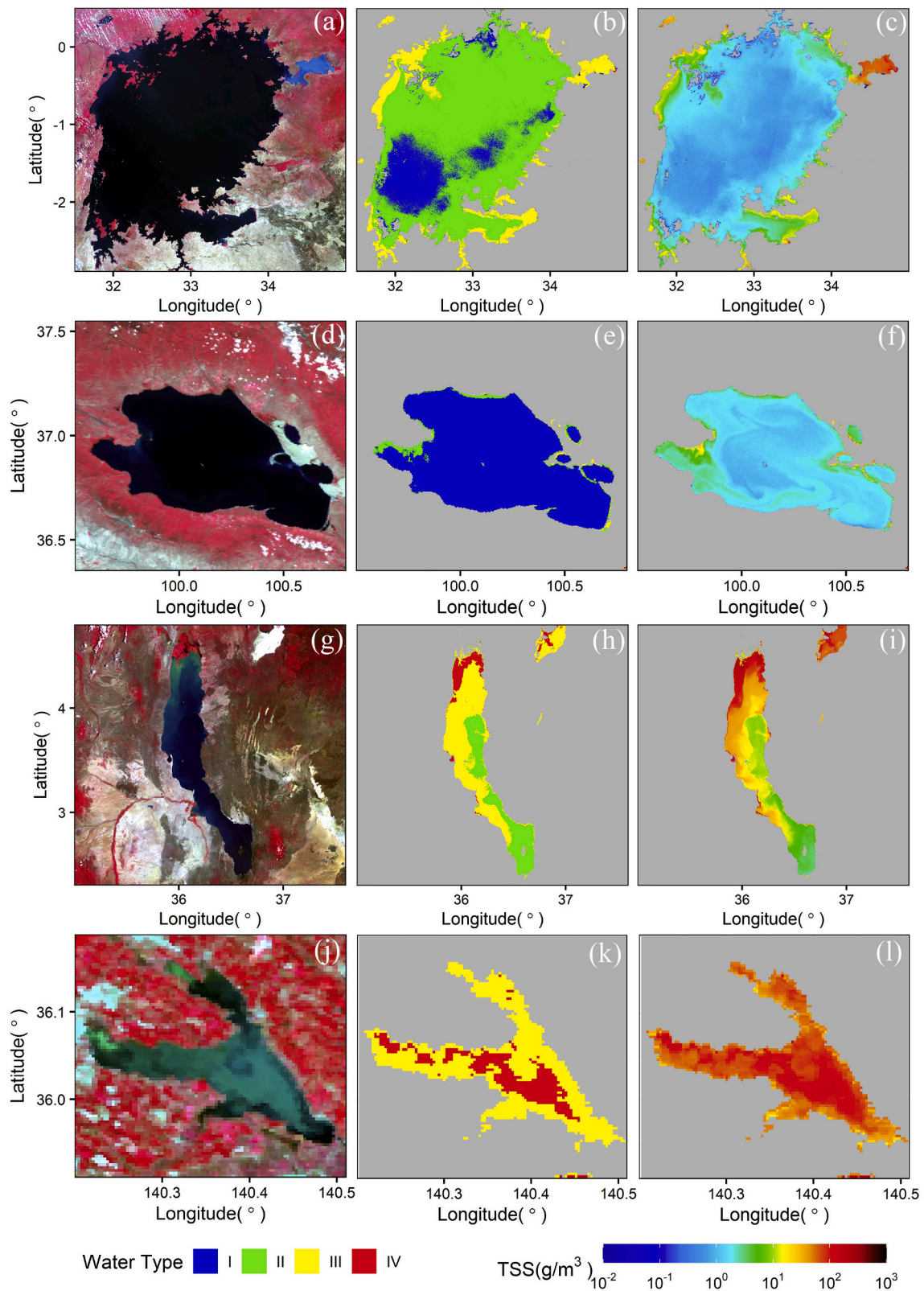
Fig. 13. Showcase maps showing the RGB OLCI image, the water type classification map, and the estimated TSS values for: (a)-(c) Lake Victoria (Aug. 17, 2016), (d)-(f) Lake Qinghai (Jun. 29, 2020), (g)-(i) Lake Turkana (Mar. 13, 2020), and (j)-(l) Lake Kasumigaura (Oct. 13, 2019).

R_{rs} differed from the *in situ*-measured R_{rs} spectra in Lake Akan and Lake Vieux Desert, and the values of R_{rs} at the selected band (560 nm) are obviously lower than *in situ*-measured R_{rs} (Fig. 15b and c). Therefore, the OLCI-derived TSS concentrations in these two lakes were underestimated (pink and yellow points in Fig. 9). However, there were some cases where the atmospherically corrected R_{rs} had similar magnitude and shape to that of *in situ* measured R_{rs} spectra. For example, the shape of OLCI atmospherically corrected R_{rs} is similar to the *in situ*-
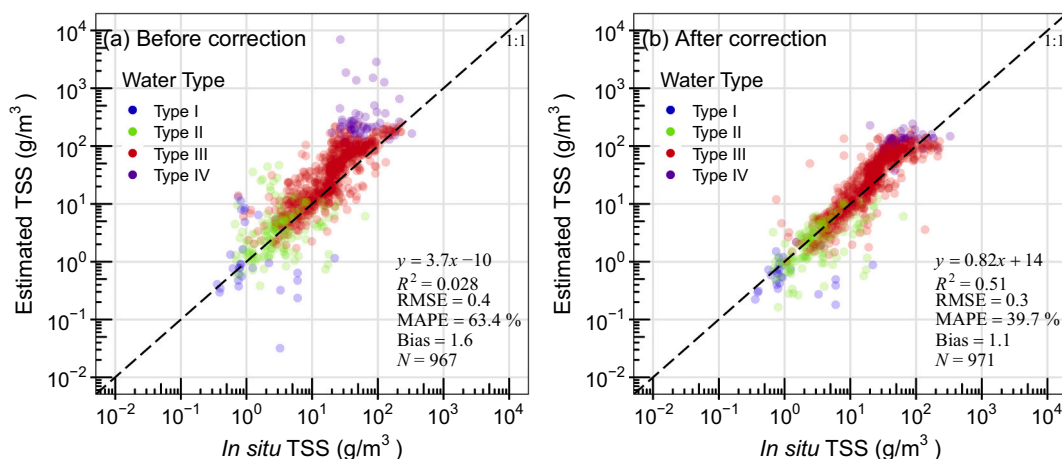
Fig. 14. Comparison of *in situ*-measured and estimated TSS values only for using *in situ*-measured R_{rs} spectra collected by the above-water approach. (a) TSS estimations using R_{rs} spectra before residual reflected skylight correction. (b) TSS estimations using R_{rs} spectra after residual reflected skylight correction.
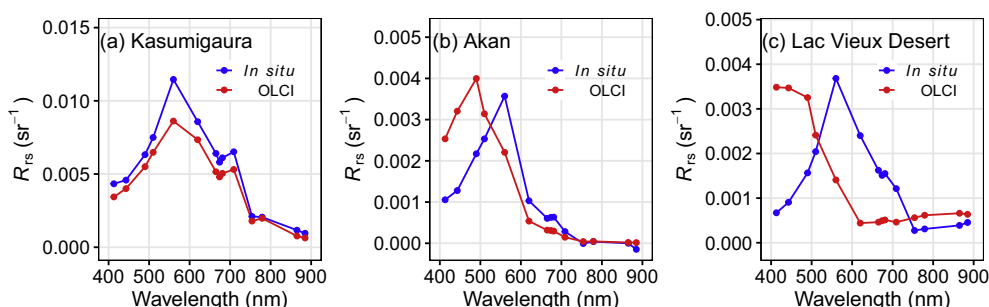

Fig. 15. Examples of comparisons between *in situ*-measured R_{rs} (blue line) and atmospherically corrected-OLCI R_{rs} (red line) acquired on the same day. (a) center of Lake Kasumigaura, Japan (2018/05/11); (b) center of Lake Akan, Japan (2019/08/27); and (c) center of Lake Vieux Desert, North America (2016/06/28). (For interpretation of the references to colour in this figure legend, the reader is referred to the web version of this article.)

measured R_{rs} spectra in Lake Kasumigaura, and the value of R_{rs} at the selected band (754 nm) for TSS estimation is very close to *in situ*-measured R_{rs} (Fig. 15a). Therefore, the OLCI-derived TSS estimations agreed well with *in situ* TSS in Lake Kasumigaura (green points in Fig. 9). Additional improvements to atmospheric corrections should ensure more accurate R_{rs} estimates from satellite images.

Although we used a one-pixel buffer along the shoreline to minimize land effects, adjacency effects are considered to be another error source for obtaining accurate R_{rs} and thus accurate TSS estimations from satellite images. The Improved Contrast between Ocean and Land (ICOL) processor available in BEAM can be used to correct the adjacency effects for improving the retrieval of R_{rs} from satellite data (Odermatt et al., 2010). This issue will be further investigated in future study.

5.3. Significance of TSS estimation from satellite imagery

Lake Kasumigaura and Lake Suwa are two of the most intensively monitored lakes in Japan (National Institute for Environmental Studies, 2020, personal communication). Even so, only monthly or weekly monitoring data at several sites are provided by the field surveys. In contrast, satellite images provide frequent water quality data (*e.g.*, Figs. 10 and 11), allowing us to capture more episodic events. For example, during April 2016 – March 2020 in Lake Kasumigaura, only 48 *in situ* TSS samples were collected by NIES for each monitoring site, but more than 370 TSS estimates were obtained from OLCI images in the same period (Fig. 10). An extreme TSS event occurred when Typhoon Hagibis made landfall in Japan on October 12, 2019. This event was accurately captured by an OLCI image acquired on October 13, 2019 (Fig. 13l), but no *in situ* TSS data was collected during the same time

period. Generally, field surveys are not carried out under strong winds, and thus these high TSS events cannot be monitored.

Importantly, satellite images can provide detailed spatial distribution maps for a wide range of TSS concentrations (Figs. 12 and 13), which can help us efficiently monitor water quality, assess the aquatic ecosystem status, and take management actions.

6. Conclusions

In this study, we propose a widely applicable method based on a semi-analytically derived b_{bp} for estimating TSS concentrations in clear to extremely turbid waters. The new method employs four wavelengths to estimate TSS concentration in clear (Type I, 560 nm), moderately turbid (Type II, 665 nm), highly turbid (Type III, 754 nm), and extremely turbid (Type IV, 865 nm) waters, respectively. The choice of an optimal wavelength (band) for different water types can not only satisfy the key assumption of $a \approx a_w$ at the core of the semi-analytical algorithm, but also ensures a TSS-sensitive wavelength for TSS retrievals, and thus allows the proposed method to work seamlessly over a wide range of turbidity levels. The validations using 1000 simulated data points (TSS ranging from 0.01 g/m³ to 1100 g/m³) and 3421 *in situ* data points (TSS ranging from 0.09 g/m³ to 2627 g/m³) confirmed the above findings. The proposed TSS estimation method, with the smallest RMSE and MAPE values (RMSE = 0.1 and MAPE = 16.0% for simulation data, RMSE = 0.3 and MAPE = 39.7% for *in situ* data), outperformed other state-of-the-art methods. The proposed TSS estimation method was also applied to MERIS and OLCI satellite images over Lake Kasumigaura and Lake Suwa, Japan for a long-term period (2003–2020). The results not only showed good agreement between the satellite-derived

and *in situ*-measured TSS values, but also demonstrated that monitoring of TSS can be enhanced using satellite data in combination with field surveys.

Declaration of Competing Interest

The authors declare that they have no known competing financial interests or personal relationships that could have appeared to influence the work reported in this paper.

Acknowledgements

References

Ahn, Y.H., Bricaud, A., Morel, A., 1992. Light backscattering efficiency and related properties of some phytoplankters. Deep Sea research part a. Oceanogr. Res. Pap. 39 (11–12), 1835–1855.

Alcàntara, E., Curtarelli, M., Stech, J., 2016. Estimating total suspended matter using the particle backscattering coefficient: results from the Itumbiara hydroelectric reservoir (Goiás state, Brazil). Remote Sensing Lett. 7 (4), 397–406.

Alikas, K., Ansko, I., Vabson, V., Ansper, A., Kangro, K., Uudeberg, K., Ligi, M., 2020. Consistency of radiometric satellite data over lakes and coastal waters with local field measurements. Remote Sens. 12 (4), 616. https://doi.org/10.3390/rs12040616.

APHA 2540, 2005. In: Eaton, A.D., Clesceri, L.S., Rice, E.W., Greenberg, A.E. (Eds.), Standard Methods for the Examination of Water and Wastewater, 21st ed. American Public Health Association, American Water Works Association, Water Environment Federation.

Balasubramanian, S.V., Pahlevan, N., Smith, B., Binding, C., Schalles, J., Loisel, H., Bunkei, M., 2020. Robust algorithm for estimating total suspended solids (TSS) in inland and nearshore coastal waters. Remote Sens. Environ. 111768.

Bilotta, G.S., Brazier, R.E., 2008. Understanding the influence of suspended solids on water quality and aquatic biota. Water Res. 42 (12), 2849–2861.

Binding, C.E., Jerome, J.H., Bukata, R.P., Booty, W.G., 2010. Suspended particulate matter in Lake Erie derived from MODIS aquatic colour imagery. Int. J. Remote Sens. 31 (19), 5239–5255.

Binding, C.E., Zastepa, A., Zeng, C., 2019. The impact of phytoplankton community composition on optical properties and satellite observations of the 2017 western Lake Erie algal bloom. J. Great Lakes Res. 45 (3), 573–586.

Bricaud, A., Morel, A., Prieur, L., 1983. Optical efficiency factors of some phytoplankters 1. Limnol. Oceanogr. 28 (5), 816–832.

Chen, S., Han, L., Chen, X., Li, D., Sun, L., Li, Y., 2015. Estimating wide range total suspended solids concentrations from MODIS 250-m imageries: an improved method. ISPRS J. Photogramm. Remote Sens. 99, 58–69.

Dekker, A.G., Vos, R.J., Peters, S.W.M., 2001. Comparison of remote sensing data, model results and in situ data for total suspended matter (TSM) in the southern Frisian lakes. Sci. Total Environ. 268 (1–3), 197–214.

Dogliotti, A.I., Ruddick, K.G., Nechad, B., Doxaran, D., Knaeps, E., 2015. A single algorithm to retrieve turbidity from remotely-sensed data in all coastal and estuarine waters. Remote Sens. Environ. 156, 157–168.

Doxaran, D., Froidefond, J.M., Castaing, P., 2002. A reflectance band ratio used to estimate suspended matter concentrations in sediment-dominated coastal waters. Int. J. Remote Sens. 23 (23), 5079–5085.

Fichot, C.G., Sathyendranath, S., Miller, W.L., 2008. SeaUV and SeaUVC: algorithms for the retrieval of UV/visible diffuse attenuation coefficients from ocean color. Remote Sens. Environ. 112 (4), 1584–1602.

Fichot, C.G., Downing, B.D., Bergamaschi, B.A., Windham-Myers, L., Marvin-DiPasquale, M., Thompson, D.R., Gierach, M.M., 2016. High-resolution remote sensing of water quality in the San Francisco Bay–Delta estuary. Environ. Sci. Technol. 50 (2), 573–583.

Fritz, C., Dörnhöfer, K., Schneider, T., Geist, J., Oppelt, N., 2017. Mapping submerged aquatic vegetation using RapidEye satellite data: the example of Lake Kummerow (Germany). Water 9 (7), 510.

Giardino, C., Brando, V.E., Dekker, A.G., Strömbeck, N., Candiani, G., 2007. Assessment of water quality in Lake Garda (Italy) using Hyperion. Remote Sens. Environ. 109 (2), 183–195.

Gitelson, A.A., Gurlin, D., Moses, W.J., Barrow, T., 2009. A bio-optical algorithm for the remote estimation of the chlorophyll-a concentration in case 2 waters. Environ. Res. Lett. 4 (4), 045003.

Gordon, H.R., Brown, O.B., Evans, R.H., Brown, J.W., Smith, R.C., Baker, K.S., Clark, D. K., 1988. A semianalytic radiance model of ocean color. J. Geophys. Res.-Atmos. 93 (D9), 10909–10924.

Groetsch, P.M., Gege, P., Simis, S.G., Eleveld, M.A., Peters, S.W., 2017. Validation of a spectral correction procedure for sun and sky reflections in above-water reflectance measurements. Opt. Express 25 (16), A742–A761.

Gurlin, D., Gitelson, A.A., Moses, W.J., 2011. Remote estimation of chl-a concentration in turbid productive waters—return to a simple two-band NIR-red model? Remote Sens. Environ. 115 (12), 3479–3490.

Han, B., Loisel, H., Vantrepotte, V., Mériaux, X., Bryère, P., Ouillon, S., Zhu, J., 2016. Development of a semi-analytical algorithm for the retrieval of suspended particulate matter from remote sensing over clear to very turbid waters. Remote Sens. 8 (3), 211.

Hou, X., Feng, L., Duan, H., Chen, X., Sun, D., Shi, K., 2017. Fifteen-year monitoring of the turbidity dynamics in large lakes and reservoirs in the middle and lower basin of the Yangtze River, China. Remote Sens. Environ. 190, 107–121.

IOCCG, 2006. Remote sensing of inherent optical properties: fundamentals, tests of algorithms, and applications. In: Lee, Z.-P. (Ed.), Reports of the International Ocean-Colour Coordinating Group, No. 5, IOCCG, Dartmouth, Canada.

IOCCG, 2014. Update of the Quasi-Analytical Algorithm (QAA_v6). Available online. http://www.ioccg.org/groups/Software_OCA/QAA_v6_2014209.pdf.

Jiang, D., Matsushita, B., Setiawan, F., Vundo, A., 2019. An improved algorithm for estimating the Secchi disk depth from remote sensing data based on the new underwater visibility theory. ISPRS J. Photogramm. Remote Sens. 152, 13–23.

Jiang, D., Matsushita, B., Yang, W., 2020. A simple and effective method for removing residual reflected skylight in above-water remote sensing reflectance measurements. ISPRS J. Photogramm. Remote Sens. 165, 16–27.

Kirk, J.T., 2011. Light and Photosynthesis in Aquatic Ecosystems. Cambridge University Press.

Knaeps, E., Ruddick, K.G., Doxaran, D., Dogliotti, A.I., Nechad, B., Raymaekers, D., Sterckx, S., 2015. A SWIR based algorithm to retrieve total suspended matter in extremely turbid waters. Remote Sens. Environ. 168, 66–79.

Knaeps, E., Doxaran, D., Dogliotti, A., Nechad, B., Ruddick, K., Raymaekers, D., Sterckx, S., 2018. The SeaSWIR dataset. Earth Syst. Sci. Data 10 (3), 1439–1449.

Kou, L., Labrie, D., Chylek, P., 1993. Refractive indices of water and ice in the 0.65- to 2.5-μm spectral range. Appl. Opt. 32 (19), 3531–3540.

Kroon, F.J., Kuhnert, P.M., Henderson, B.L., Wilkinson, S.N., Kinsey-Henderson, A., Abbott, B., Turner, R.D., 2012. River loads of suspended solids, nitrogen, phosphorus and herbicides delivered to the great barrier reef lagoon. Mar. Pollut. Bull. 65 (4–9), 167–181.

Kutser, T., Herlevi, A., Kallio, K., Arst, H., 2001. A hyperspectral model for interpretation of passive optical remote sensing data from turbid lakes. Sci. Total Environ. 268 (1–3), 47–58.

Kutser, T., Metsamaa, L., Vahtmäe, E., Aps, R., 2007. Operative monitoring of the extent of dredging plumes in coastal ecosystems using MODIS satellite imagery. J. Coast. Res. 180–184.

Kutser, T., Vahtmäe, E., Paavel, B., Kauer, T., 2013. Removing glint effects from field radiometry data measured in optically complex coastal and inland waters. Remote Sens. Environ. 133, 85–89.

Lee, Z., Carder, K.L., Arnone, R.A., 2002. Deriving inherent optical properties from water color: a multiband quasi-analytical algorithm for optically deep waters. Appl. Opt. 41 (27), 5755–5772.

Lee, Z., Ahn, Y.H., Mobley, C., Arnone, R., 2010. Removal of surface-reflected light for the measurement of remote-sensing reflectance from an above-surface platform. Opt. Express 18 (25), 26313–26324.

Lee, Z., Pahlevan, N., Ahn, Y.H., Greb, S., O'Donnell, D., 2013. Robust approach to directly measuring water-leaving radiance in the field. Appl. Opt. 52 (8), 1693–1701.

Mao, Z., Chen, J., Pan, D., Tao, B., Zhu, Q., 2012. A regional remote sensing algorithm for total suspended matter in the East China Sea. Remote Sens. Environ. 124, 819–831.

Matsushita, B., Yang, W., Yu, G., Oyama, Y., Yoshimura, K., Fukushima, T., 2015. A hybrid algorithm for estimating the chlorophyll-a concentration across different trophic states in Asian inland waters. ISPRS J. Photogramm. Remote Sens. 102, 28–37.

Miller, R.L., McKee, B.A., 2004. Using MODIS Terra 250 m imagery to map concentrations of total suspended matter in coastal waters. Remote Sens. Environ. 93 (1–2), 259–266.

Mitchell, B.G., 1990. Algorithms for determining the absorption coefficient for aquatic particulates using the quantitative filter technique. In: Ocean optics X, vol. 1302. International Society for Optics and Photonics, pp. 137–148.

Mobley, C.D., 1994. Light and Water: Radiative Transfer in Natural Waters. Academic press.

Mobley, C.D., 1999. Estimation of the remote-sensing reflectance from above-surface measurements. Appl. Opt. 38 (36), 7442–7455.

Moore, T.S., Dowell, M.D., Bradt, S., Verdu, A.R., 2014. An optical water type framework for selecting and blending retrievals from bio-optical algorithms in lakes and coastal waters. Remote Sens. Environ. 143, 97–111.

National Institute for Environmental Studies, 2020. Lake Kasumigaura Database, National Institute for Environmental Studies, Japan. Accessed via. http://db.cger.nies.go.jp/gem/moni-e/inter/GEMS/database/kasumi/index.html. on 24-08-2020.

Nechad, B., Ruddick, K.G., Park, Y., 2010. Calibration and validation of a generic multisensor algorithm for mapping of total suspended matter in turbid waters. Remote Sens. Environ. 114 (4), 854–866.

Neil, C., Spyrakos, E., Hunter, P.D., Tyler, A.N., 2019. A global approach for chlorophyll-a retrieval across optically complex inland waters based on optical water types. Remote Sens. Environ. 229, 159–178.

Neukermans, G., Loisel, H., Mériaux, X., Astoreca, R., McKee, D., 2012. In situ variability of mass-specific beam attenuation and backscattering of marine particles with respect to particle size, density, and composition. Limnol. Oceanogr. 57 (1), 24–144.

Novoa, S., Doxaran, D., Ody, A., Vanhellemont, Q., Lafon, V., Lubac, B., Gernez, P., 2017. Atmospheric corrections and multi-conditional algorithm for multi-sensor remote sensing of suspended particulate matter in low-to-high turbidity levels coastal waters. Remote Sens. 9 (1), 61.

Odermatt, D., Giardino, C., Heege, T., 2010. Chlorophyll retrieval with MERIS Case-2-regional in perialpine lakes. Remote Sens. Environ. 114, 607–617.

Ondrusek, M., Stengel, E., Kinkade, C.S., Vogel, R.L., Keegstra, P., Hunter, C., Kim, C., 2012. The development of a new optical total suspended matter algorithm for the Chesapeake Bay. Remote Sens. Environ. 119, 243–254.

Östlund, C., Flink, P., Strömbeck, N., Pierson, D., Lindell, T., 2001. Mapping of the water quality of Lake Erken, Sweden, from imaging spectrometry and Landsat thematic mapper. Sci. Total Environ. 268 (1–3), 139–154.

Oyama, Y., Matsushita, B., Fukushima, T., Matsushige, K., Imai, A., 2009. Application of spectral decomposition algorithm for mapping water quality in a turbid lake (Lake Kasumigaura, Japan) from Landsat TM data. ISPRS J. Photogramm. Remote Sens. 64 (1), 73–85.

Pope, R.M., Fry, E.S., 1997. Absorption spectrum (380–700 nm) of pure water. II. Integrating cavity measurements. Appl. Opt. 36 (33), 8710–8723.

Reinart, A., Paavel, B., Pierson, D., Strombeck, N., 2004. Inherent and apparent optical properties of Lake Peipsi, Estonia. Boreal Environ. Res. 9 (5), 429–445.

Ruddick, K., De Cauwer, V., Van Mol, B., 2005. Use of the near infrared similarity reflectance spectrum for the quality control of remote sensing data. In: Remote Sensing of the Coastal Oceanic Environment. International Society for Optics and Photonics.

Salem, S.I., Higa, H., Kim, H., Kazuhiro, K., Kobayashi, H., Oki, K., Oki, T., 2017. Multi-algorithm indices and look-up table for chlorophyll-a retrieval in highly turbid water bodies using multispectral data. Remote Sens. 9 (6), 556.

Schalles, J.F., 2006. Optical remote sensing techniques to estimate phytoplankton chlorophyll a concentrations in coastal waters with varying suspended matter and CDOM concentrations. In: Richardson, L., Ledrew, E. (Eds.), Remote Sensing of Aquatic Coastal Ecosystem Processes: Science and Management Applications. Springer, pp. 27–79.

Shang, Z., Lee, Z., Dong, Q., Wei, J., 2017. Self-shading associated with a skylight-blocked approach system for the measurement of water-leaving radiance and its correction. Appl. Opt. 56 (25), 7033–7040.

Shi, K., Zhang, Y.L., Zhu, G.W., Liu, X.H., Zhou, Y.Q., Xu, H., Qin, B.Q., Liu, G., Li, Y.M., 2015. Long-term remote monitoring of total suspended matter concentration in Lake Taihu using 250 m MODIS-aqua data. Remote Sens. Environ. 164, 43–56.

Strickland, J.D.H., Parsons, T.R., 1972. A practical hand book of seawater analysis. In: Fisheries research Board of Canada Bulletin, , 2nd ed.157, p. 310.

Strömbeck, N., Pierson, D.C., 2001. The effects of variability in the inherent optical properties on estimations of chlorophyll a by remote sensing in Swedish freshwaters. Sci. Total Environ. 268 (1–3), 123–137.

Syvitski, J.P., Vörösmarty, C.J., Kettner, A.J., Green, P., 2005. Impact of humans on the flux of terrestrial sediment to the global coastal ocean. Science 308 (5720), 376–380.

Thompson, D.R., Gao, B.-C., Green, R.O., Roberts, D.A., Dennison, P.E., Lundeen, S.R., 2015. Atmospheric correction for global mapping spectroscopy: ATREM advances for the HyspIRI preparatory campaign. Remote Sens. Environ. 167, 64–77.

Vahtmäe, E., Kutser, T., Martin, G., Kotta, J., 2006. Feasibility of hyperspectral remote sensing for mapping benthic macroalgal cover in turbid coastal waters—a Baltic Sea case study. Remote Sens. Environ. 101 (3), 342–351.

Vaillancourt, R.D., Brown, C.W., Guillard, R.R.L., Balch, W.M., 2004. Light backscattering properties of marine phytoplankton: relationships to cell size, chemical composition and taxonomy. J. Plankton Res. 26 (2), 191–212.

Vantrepotte, V., Loisel, H., Dessailly, D., Mériaux, X., 2012. Optical classification of contrasted coastal waters. Remote Sens. Environ. 123, 306–323.

Williamson, T.N., Crawford, C.G., 2011. Estimation of suspended-sediment concentration from Total suspended solids and turbidity data for Kentucky, 1978-1995 1. J. Am. Water Res. Assoc. 47 (4), 739–749.

Xue, K., Boss, E., Ma, R., Shen, M., 2019. Algorithm to derive inherent optical properties from remote sensing reflectance in turbid and eutrophic lakes. Appl. Opt. 58 (31), 8549–8564.

Xue, K., Ma, R., Shen, M., Li, Y., Duan, H., Cao, Z., Xiong, J., 2020. Variations of suspended particulate concentration and composition in Chinese lakes observed from Sentinel-3A OLCI images. Sci. Total Environ. 137774.

Yang, W., Matsushita, B., Chen, J., Fukushima, T., 2011. Estimating constituent concentrations in case II waters from MERIS satellite data by semi-analytical model optimizing and look-up tables. Remote Sens. Environ. 115 (5), 1247–1259.

Yang, W., Matsushita, B., Chen, J., Yoshimura, K., Fukushima, T., 2013. Retrieval of inherent optical properties for turbid inland waters from remote-sensing reflectance. IEEE Trans. Geosci. Remote Sens. 51 (6), 3761–3773.

Yu, X., Lee, Z., Shen, F., Wang, M., Wei, J., Jiang, L., Shang, Z., 2019. An empirical algorithm to seamlessly retrieve the concentration of suspended particulate matter from water color across ocean to turbid river mouths. Remote Sens. Environ. 235, 111491.

Zhang, X., Hu, L., He, M.X., 2009. Scattering by pure seawater: effect of salinity. Opt. Express 17 (7), 5698–5710.

Zhang, M., Tang, J., Dong, Q., Song, Q., Ding, J., 2010. Retrieval of total suspended matter concentration in the yellow and East China seas from MODIS imagery. Remote Sens. Environ. 114 (2), 392–403.